



Silicon-Chip-Based Optical Frequency Combs

Alexander Gaeta
CORNELL UNIVERSITY

10/26/2015
Final Report

DISTRIBUTION A: Distribution approved for public release.

Air Force Research Laboratory
AF Office Of Scientific Research (AFOSR)/ RTB1
Arlington, Virginia 22203
Air Force Materiel Command

REPORT DOCUMENTATION PAGE					Form Approved OMB No. 0704-0188							
<p>The public reporting burden for this collection of information is estimated to average 1 hour per response, including the time for reviewing instructions, searching existing data sources, gathering and maintaining the data needed, and completing and reviewing the collection of information. Send comments regarding this burden estimate or any other aspect of this collection of information, including suggestions for reducing the burden, to the Department of Defense, Executive Service Directorate (0704-0188). Respondents should be aware that notwithstanding any other provision of law, no person shall be subject to any penalty for failing to comply with a collection of information if it does not display a currently valid OMB control number.</p> <p>PLEASE DO NOT RETURN YOUR FORM TO THE ABOVE ORGANIZATION.</p>												
1. REPORT DATE (DD-MM-YYYY) 14-10-2015		2. REPORT TYPE Final			3. DATES COVERED (From - To) 15-07-2012 to 14-07-2015							
4. TITLE AND SUBTITLE SILICON-CHIP-BASED OPTICAL FREQUENCY COMBS				5a. CONTRACT NUMBER								
				5b. GRANT NUMBER FA9550-12-1-0377								
				5c. PROGRAM ELEMENT NUMBER								
6. AUTHOR(S) Gaeta, Alexander, L Lipson, Michal				5d. PROJECT NUMBER								
				5e. TASK NUMBER								
				5f. WORK UNIT NUMBER								
7. PERFORMING ORGANIZATION NAME(S) AND ADDRESS(ES) CORNELL UNIVERSITY, INC OFFICE OF SPONSORED PROGRAMS 373 PINE TREE RD ITHACA NY 14850-2820					8. PERFORMING ORGANIZATION REPORT NUMBER 67172/A001							
9. SPONSORING/MONITORING AGENCY NAME(S) AND ADDRESS(ES) USAF, AFRL DUNS 143574726 AF OFFICE OF SCIENTIFIC RESEARCH 875 NORTH RANDOLPH STREET, RM 3112 ARLINGTON VA 22203					10. SPONSOR/MONITOR'S ACRONYM(S)							
					11. SPONSOR/MONITOR'S REPORT NUMBER(S)							
12. DISTRIBUTION/AVAILABILITY STATEMENT Approve for public release.												
13. SUPPLEMENTARY NOTES												
14. ABSTRACT We have theoretically and experimentally investigated the dynamics of frequency comb generation in silicon-based microresonators. In this system, the parametric gain associated with the nonlinear process of four-wave mixing leads to parametric oscillation and generation of signal/idler sidemodes. This report describes our results that further develop the parametric comb technology. We theoretically investigate comb generation and modelocking dynamics, and the connection to concepts of synchronization and self-organization. We also investigated mode-crossings in microresonators and tunable coupling, and their impact on comb formation. We studied comb generation without an external pump laser. In addition, we explored comb generation at other pump wavelengths using dispersion engineering. Finally, we investigated comb generation via coherent supercontinuum generation in silicon nitride waveguides.												
15. SUBJECT TERMS Nonlinear optics, parametric mixing, nanophotonics, optical frequency combs												
16. SECURITY CLASSIFICATION OF: <table border="1" style="width: 100%; border-collapse: collapse;"> <tr> <td style="width: 33%; padding: 2px;">a. REPORT</td> <td style="width: 33%; padding: 2px;">b. ABSTRACT</td> <td style="width: 33%; padding: 2px;">c. THIS PAGE</td> </tr> <tr> <td style="text-align: center; padding: 2px;">U</td> <td style="text-align: center; padding: 2px;">U</td> <td style="text-align: center; padding: 2px;">U</td> </tr> </table>			a. REPORT	b. ABSTRACT	c. THIS PAGE	U	U	U	17. LIMITATION OF ABSTRACT UU		18. NUMBER OF PAGES 40	
a. REPORT	b. ABSTRACT	c. THIS PAGE										
U	U	U										
			19a. NAME OF RESPONSIBLE PERSON Alexander Gaeta									
			19b. TELEPHONE NUMBER (Include area code) 607-592-8863									

Reset

INSTRUCTIONS FOR COMPLETING SF 298

1. REPORT DATE. Full publication date, including day, month, if available. Must cite at least the year and be Year 2000 compliant, e.g. 30-06-1998; xx-06-1998; xx-xx-1998.

2. REPORT TYPE. State the type of report, such as final, technical, interim, memorandum, master's thesis, progress, quarterly, research, special, group study, etc.

3. DATES COVERED. Indicate the time during which the work was performed and the report was written, e.g., Jun 1997 - Jun 1998; 1-10 Jun 1996; May - Nov 1998; Nov 1998.

4. TITLE. Enter title and subtitle with volume number and part number, if applicable. On classified documents, enter the title classification in parentheses.

5a. CONTRACT NUMBER. Enter all contract numbers as they appear in the report, e.g. F33615-86-C-5169.

5b. GRANT NUMBER. Enter all grant numbers as they appear in the report, e.g. AFOSR-82-1234.

5c. PROGRAM ELEMENT NUMBER. Enter all program element numbers as they appear in the report, e.g. 61101A.

5d. PROJECT NUMBER. Enter all project numbers as they appear in the report, e.g. 1F665702D1257; ILIR.

5e. TASK NUMBER. Enter all task numbers as they appear in the report, e.g. 05; RF0330201; T4112.

5f. WORK UNIT NUMBER. Enter all work unit numbers as they appear in the report, e.g. 001; AFAPL30480105.

6. AUTHOR(S). Enter name(s) of person(s) responsible for writing the report, performing the research, or credited with the content of the report. The form of entry is the last name, first name, middle initial, and additional qualifiers separated by commas, e.g. Smith, Richard, J, Jr.

7. PERFORMING ORGANIZATION NAME(S) AND ADDRESS(ES). Self-explanatory.

8. PERFORMING ORGANIZATION REPORT NUMBER. Enter all unique alphanumeric report numbers assigned by the performing organization, e.g. BRL-1234; AFWL-TR-85-4017-Vol-21-PT-2.

9. SPONSORING/MONITORING AGENCY NAME(S) AND ADDRESS(ES). Enter the name and address of the organization(s) financially responsible for and monitoring the work.

10. SPONSOR/MONITOR'S ACRONYM(S). Enter, if available, e.g. BRL, ARDEC, NADC.

11. SPONSOR/MONITOR'S REPORT NUMBER(S). Enter report number as assigned by the sponsoring/monitoring agency, if available, e.g. BRL-TR-829; -215.

12. DISTRIBUTION/AVAILABILITY STATEMENT. Use agency-mandated availability statements to indicate the public availability or distribution limitations of the report. If additional limitations/ restrictions or special markings are indicated, follow agency authorization procedures, e.g. RD/FRD, PROPIN, ITAR, etc. Include copyright information.

13. SUPPLEMENTARY NOTES. Enter information not included elsewhere such as: prepared in cooperation with; translation of; report supersedes; old edition number, etc.

14. ABSTRACT. A brief (approximately 200 words) factual summary of the most significant information.

15. SUBJECT TERMS. Key words or phrases identifying major concepts in the report.

16. SECURITY CLASSIFICATION. Enter security classification in accordance with security classification regulations, e.g. U, C, S, etc. If this form contains classified information, stamp classification level on the top and bottom of this page.

17. LIMITATION OF ABSTRACT. This block must be completed to assign a distribution limitation to the abstract. Enter UU (Unclassified Unlimited) or SAR (Same as Report). An entry in this block is necessary if the abstract is to be limited.

Table of Contents

<u>Section</u>	<u>Page</u>
1. Abstract	2
2. Introduction	3
3. Modeling Parametric Frequency Comb Generation	4
4. Self-Organization in Soliton Modelocked Parametric Frequency Combs.....	9
5. Mode Coupling in Microresonators	12
6. Tunable Frequency Combs using Dual-Microring Resonators	15
7. Microresonator-Based Comb Generation Without an External Laser Source.....	20
8. Frequency Comb Generation Near Visible Wavelengths	23
9. Frequency Comb Generation in the Mid-Infrared	28
10. Supercontinuum Generation in Si-Based Nanowaveguides	31
11. References	35

1. Abstract

We have theoretically and experimentally investigated the dynamics of frequency comb generation in silicon-based microresonators. In this system, the parametric gain associated with the nonlinear process of four-wave mixing leads to parametric oscillation and generation of signal/idler sidemodes. This report describes our results that further develop the parametric comb technology. We theoretically investigate comb generation and modelocking dynamics, and the connection to concepts of synchronization and self-organization. We also investigated mode-crossings in microresonators and tunable coupling, and their impact on comb formation. We studied comb generation without an external pump laser. In addition, we explored comb generation at other pump wavelengths using dispersion engineering. Finally, we investigated comb generation via coherent supercontinuum generation in silicon nitride waveguides.

Our research effort illustrates that the silicon-based platform offers a high potential as a platform for robust, integrated, chip-scale comb source. Since the dispersion of the system can be readily tailored through waveguide cross-section engineering, the platform offers flexibility in operating wavelength and bandwidth. The developments made here are a significant step towards the development of chip-based frequency combs that can operate in real-world sensing and spectroscopy, for optical clocks, and for frequency metrology applications.

2. Introduction

Over the past decade, there has been tremendous development in the development of techniques for producing optical frequency combs [1], with applications including spectroscopy, optical clocks, arbitrary waveform generation, frequency metrology, and astronomical spectrograph calibration [2,3,4]. Traditionally, modelocked solid-state and fiber lasers have been used for optical frequency comb generation. For full self-stabilization of frequency combs, it is desirable to have a broadband, octave-spanning spectrum for stabilizing the carrier-envelope offset frequency f_{CEO} , which is one of the two degrees of freedom. Using an f - $2f$ interferometer, the low-frequency component of the comb is doubled and heterodyned with the high-frequency component, allowing for extraction of the f_{CEO} , which can be locked to a microwave frequency standard [5]. The other degree of freedom is the comb spacing, or the repetition frequency f_{rep} , which can be directly detected and referenced to a frequency standard, such that the m^{th} comb line has frequency $f_m = f_{\text{CEO}} + mf_{\text{R}}$.

However, a novel approach to producing frequency combs has emerged in the past 10 years through the use of parametric nonlinear interactions in microresonators [6,7]. In this approach, a single CW laser beam coupled to a microresonators can produce stabilized, octave-spanning combs through highly cascaded four-wave mixing (FWM) oscillation and soliton modelocking. The tight transverse confinement of the light within these resonators enables operation at modest CW pump powers and powerful dispersion engineering that allows the for the creation of anomalous dispersion over a wide range of wavelength ranges necessary to produce ultrabroadband combs. The highly compact size of the this comb-generating system ensures that it will operate at low powers to produce combs with spacings ranging from 10 GHz to 1 THz while being highly integrated and robust and an enabling technology for many spectroscopic applications and devices. In our research, we utilize silicon nitride microresonators for parametric frequency comb generation [8,9,10,11]. Unlike many other high- Q resonator designs, the resonator and the coupling waveguide are monolithically integrated. Thus, the entire on-chip configuration of CMOS-compatible microresonators can provide robust operation in ambient conditions yielding a truly monolithic, robust, and highly compact frequency comb source.

3. Modeling Parametric Frequency Comb Generation

We use the Lugiato-Lefever (LL) model [12,13,14,15,16] to simulate the full temporal dynamics of comb generation dynamics in microresonators. We extend this model to include higher-order dispersion and self-steepening to enable simulations of comb spectra that span an octave. The LL model has demonstrated excellent agreement with experimental results when used to solve for a steady-state solution of the spectrum [14]. In our analysis we assume the mode frequencies are equally spaced, using the free-spectral range (FSR) of the pumped mode, and allow the phase of these modes to define the dispersion-induced frequency offset. Additionally, since we treat the field both in the time and frequency domains, additional terms such as higher-order dispersion, self-steepening, Raman scattering, two- and three-photon absorption, and free-carrier effects can easily be included in a manner similar to supercontinuum simulations [17]. Using this model, we identify distinct and necessary stages, including one that is chaotic and unstabilized, that yields a path to stable, single-pulse modelocking.

We express the LL equation with contributions from higher-order dispersion and self-steepening as, where E is the resonator field, E_{in} is the pump field at frequency ω_0 , t and τ are the slow and fast times, respectively, describing the slow evolution of the cavity field and temporal field within the cavity at a given time t , γ is the nonlinear parameter, L is cavity length, t_R is the round-trip time, δ_0 is the cavity detuning, α is loss per roundtrip, θ is the transmission coefficient between the resonator and the bus waveguide, and β_n is the n -th order dispersion coefficient.

$$t_R \frac{\partial E(t, \tau)}{\partial t} = \left[-\alpha - i\delta_0 + iL \sum_{n \geq 2} \frac{\beta_n}{n!} \left(i \frac{\partial}{\partial \tau} \right)^n + i\gamma L \left(1 + \frac{i}{\omega_0} \frac{\partial}{\partial \tau} \right) |E(t, \tau)|^2 \right] E(t, \tau) + \sqrt{\theta} E_{\text{in}} \quad (1)$$

Figure 1 shows a route to achieving stable, single-pulse modelocked octave-spanning frequency comb. Parameters are taken from the 226-GHz FSR Si_3N_4 microring resonator in Ref. [10]. The continuous-wave (CW) pump wavelength λ_p at 1550 nm is positioned in the anomalous group-velocity dispersion (GVD) regime between the two zero-GVD points (ZGVD's) of the waveguide ZGVD1 and ZGVD2 at 1000 nm and 1760 nm, respectively, with a pump power $P_{\text{in}} = |E_{\text{in}}|^2$ of 1.5 W. The system goes through four stages, corresponding to four different frequency detunings of the pump field. Stage I consists of the formation of multiple stable cavity solitons. At the bare-cavity detuning $\delta_0 = 0$, the resonance shifts away from the pump due to the Kerr effect as energy builds up within the ring. Anomalous GVD allows modulation instability to convert energy from the driven mode to the primary offset resonances ~ 23 modes (50 nm) away, which is dictated by phase-matching conditions [18]. Further build-up of power then causes cascaded four-wave mixing (FWM) of these MI peaks within the anomalous GVD region. Various other combination of FWM processes will also occur, which results in the formation of mini-combs. Once these mini-combs begin to overlap, the temporal characteristics change dramatically, forming stable cavity solitons as initial modelocking occurs. In Stage II, as the pump is tuned closer to the Kerr-shifted resonance, the intracavity power increases, and the multi-pulse modelocking is lost due to instability of the cavity solitons. Adjacent pulses interact with each other causing destabilization and what appears to be chaotic behavior [19]. Further detuning of the pump past the Kerr-shifted resonance in Stage III causes

the intracavity power to drop, and modelocking is again observed. After the change in δ_0 , multiple cavity solitons re-form, but only the stable ones persist. The remaining pulses collide with the nearest neighbors and annihilate, causing spikes in power and broad lines seen in the corresponding spectral evolution. In the final stage, the pump detuning is increased again. At the lower intracavity powers the remaining cavity solitons destabilize and dissipate. At the suitable pump detuning, the system evolves to a single pulse within the microresonator. The modelocked frequency comb is smooth and spans an octave across ZGVD2 into normal GVD regime, as has been observed experimentally [10], with the dispersive wave feeding energy into the longer wavelength modes.

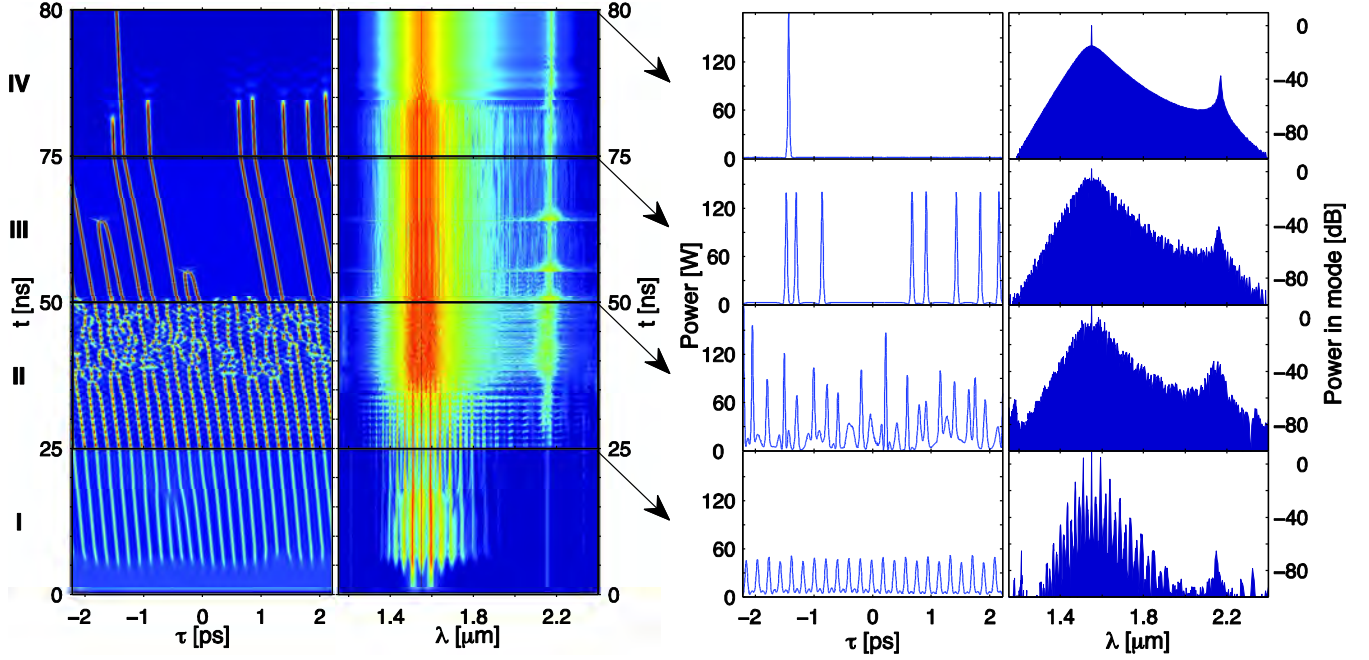


Figure 1. Evolution of single-pulse modelocking within a 226 GHz monolithic Si_3N_4 ring resonator. Each of the four stages (bottom to top) represent an increase in pump detuning from on-resonance to $\delta_0 = 0.02, 0.04, 0.05642$ at simulated times $\tau = 25, 50, 75$ ns. The pump power, $|E_{\text{in}}|^2$ is kept constant at 1.5 W. Column 1 is the temporal evolution, with power plotted on identical linear scales, and τ spanning a single roundtrip time. Column 2 is the spectral evolution, with spectral power plotted on the same 100 dB-scale. Column 3 and 4 show the temporal and spectral power, respectively, at the end of Stages I - IV.

Next, we investigate the effects of GVD, higher-order dispersion, and self-steepening on sideband generation from FWM [20] by analyzing the coupled mode equations associated with the field $E(t, \tau) = A_0 + A_+ + A_-$ [21,22,23], where A_0 is the pump field and A_+ and A_- represent the symmetrically detuned sidemodes. For our analysis, we assume that the amplitude of the sidebands are much smaller than A_0 , in which case the coupled equations are given as,

$$t_R \frac{\partial A_0}{\partial t} = -(\alpha + i\delta_0) A_0 + i\gamma L |A_0|^2 A_0 + 2i\gamma L A_0^* A_+ A_- + \sqrt{\theta} E_{\text{in}}, \quad (2)$$

$$t_R \frac{\partial A_+}{\partial t} = - \left[\alpha + i\Delta\kappa + iL \sum_{n=3,5,\dots} \frac{\beta_n}{n!} \Omega^n + 2iL \frac{\Omega}{\omega_0} \gamma |A_0|^2 \right] A_+ + i\gamma L \left(1 - \frac{\Omega}{\omega_0} \right) A_0^2 A_-^*, \quad (3)$$

$$t_R \frac{\partial A_-}{\partial t} = - \left[\alpha + i\Delta\kappa - iL \sum_{n=3,5,\dots} \frac{\beta_n}{n!} \Omega^n - 2iL \frac{\Omega}{\omega_0} \gamma |A_0|^2 \right] A_- + i\gamma L \left(1 + \frac{\Omega}{\omega_0} \right) A_0^2 A_+^*, \quad (4)$$

where Ω is the sideband detuning, and the phase mismatch is given by,

$$\Delta\kappa = \delta_0 - L \sum_{n=2,4,\dots} \frac{\beta_n}{n!} \Omega^n - 2\gamma L |A_0|^2. \quad (5)$$

The resulting solutions for A_+ and A_- are,

$$A_+(t) = A_+(0) \exp \left[\Lambda(\Omega) \frac{t}{t_R} \right] \times \exp \left[-i \left(L \sum_{n=3,5,\dots} \frac{\beta_n}{n!} \Omega^n + 2\gamma L \frac{\Omega}{\omega_0} |A_0|^2 \right) \frac{t}{t_R} \right], \quad (6)$$

$$A_-(t) = A_-(0) \exp \left[\Lambda(\Omega) \frac{t}{t_R} \right] \times \exp \left[i \left(L \sum_{n=3,5,\dots} \frac{\beta_n}{n!} \Omega^n + 2\gamma L \frac{\Omega}{\omega_0} |A_0|^2 \right) \frac{t}{t_R} \right], \quad (7)$$

where $\Lambda(\Omega) = -\alpha + \sqrt{\left[\gamma L \left(1 - \Omega^2 / \omega_0^2 \right) |A_0|^2 \right]^2 - (\Delta\kappa)^2}$ is the gain coefficient. This gain coefficient Λ and phase mismatch $\Delta\kappa$ depend on the even-orders of dispersion, while the odd-order dispersion terms add a phase contribution to the sidebands which is opposite in sign with respect to each other. While the odd-order terms do not contribute directly to the amplitude growth, these phase terms are relevant for pulse shaping and mode-locking. The inclusion of the self-steepening term does not affect $\Delta\kappa$, but modifies the nonlinear term in the gain and contributes an additional phase term.

We investigate how the comb bandwidth can be controlled using two different waveguide cross sections of 690×1900 nm and 910×1800 nm. Previously, the high stress in silicon-nitride films prevented deposition of high quality nitride films, which in turn limited the magnitude of the anomalous GVD that could be reached. However, recent advances in fabrication techniques have allowed for deposition of thick, high quality films [24], enabling higher anomalous GVD values and access to a wider parameter space for waveguide dispersion. The GVD for the Si_3N_4 waveguide is shown in Fig. 2(a) which was calculated with a finite-element mode-solver. For the comb simulations, the microring has a 100- μm radius and is pumped at 1550 nm with 650 mW in the coupling waveguide. Figure 2(b) shows the generated comb spectra for the two different dimensions. While the region of anomalous GVD for the 690×1900 nm cross section spans only 550 nm, the low anomalous GVD at the pump wavelength allows the comb to span a bandwidth far exceeding the anomalous GVD region. In contrast, for the 910×1800 nm cross section, for which the anomalous GVD region spans 1250 nm, the large anomalous GVD at the pump

wavelength results in narrowband comb generation. We find that the overall comb bandwidth that is ultimately produced is dictated in part by the frequency detuning between the pump and the first generated sideband. Considering the phase mismatch equation with only the GVD contribution, the detuning is inversely proportional to the square root of β_2 . This implies that for larger (smaller) β_2 values the smaller (larger) the frequency detuning results in a narrower (broader) bandwidth. The bandwidth dependence on GVD is consistent with the predictions based on steady-state analysis by Coen and Erkintalo [25]. Figure 2(c) shows the temporal profile of the simulated combs and indicates single-pulse modelocking and cavity soliton formation, which is indicative of a stabilized comb [11,26]. The narrower bandwidth allows for a higher power per comb line allowing for more efficient power conversion from the pump to the comb lines, which is critical for an energy-efficient multiple wavelength source for WDM applications.

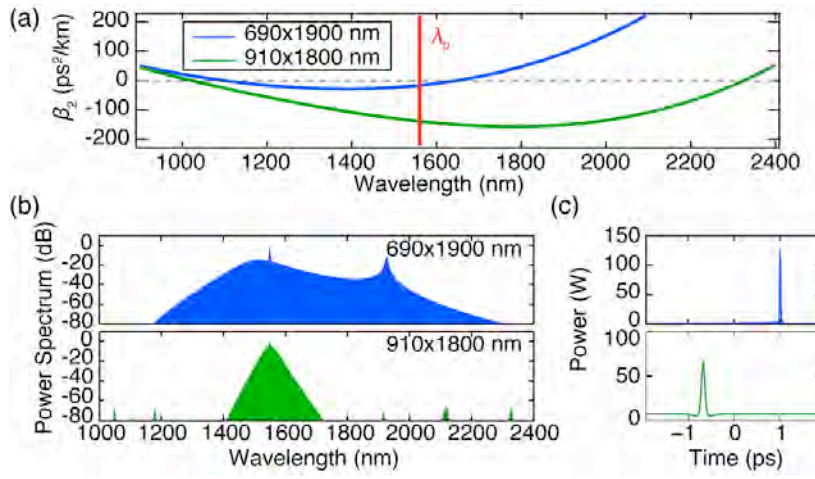


Figure 2. (a) Simulated GVD for Si_3N_4 waveguides with cross sections 690×1900 nm (blue) and 910×1800 nm (green). (b) Simulated comb spectra and (c) temporal plot for 260-GHz FSR Si_3N_4 microring resonators with cross sections 690×1900 nm (top) and 910×1800 nm (bottom).

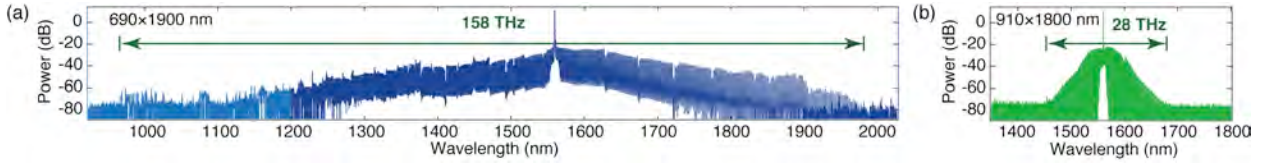


Figure 3. Measured comb spectra in Si_3N_4 microrings with cross sections (a) 690×1900 nm and (b) 910×1800 nm (green).

We investigate these predictions experimentally by pumping at a microring resonance near 1560 nm using an amplified single-frequency laser. To cover the entire spectral measurement range, we utilize two optical spectrum analyzers operating from 900 – 1200 nm and from 1200 – 2400 nm. Figures 3(a) and 3(b) show the measured spectra from the 690×1900 nm and 910×1800 nm cross-section microring, respectively. The 690×1900 nm microring [Fig. 3(a)] generates a 158-THz bandwidth comb, which represents the broadest comb generated to date in a silicon nitride platform. The additional spectral lines between 2 – 2.4 μm [shaded region in Fig. 3(a)] correspond to second-order diffraction of the comb lines generated in the 1 – 1.2 μm range

in the grating-based spectrometer. In contrast, the comb generated in the 690×1900 nm microring [Fig. 4(a)] spans a significantly narrower bandwidth of 28 THz. The bandwidths of the measured spectra are in good agreement with our theoretical predictions [Fig. 2(b)].

Next, we investigate the effects of higher-order dispersion by modeling comb generation at three different pump wavelengths, 1550 nm, 1400 nm, and 1200 nm. Figure 4(a) shows the GVD and fourth-order dispersion (FOD) for a 690×1900 nm cross section, and Fig. 4(b) shows the simulated comb spectra for each pump wavelength. In each case, a stabilized, singlepulsed modelocked comb is achieved. In comparing the comb spectra for the 1550- and 1400-nm pumps, the comb bandwidth is significantly broader for the 1400-nm pump even though the magnitude of GVD is smaller for the 1550-nm pump. This is due to the FOD contribution to phase matching, which becomes significant for FWM over broader bandwidths. The broadest comb is generated with the 1200-nm pump, where the GVD and FOD values are the lowest. While the GVD at 1200 nm ($\beta_2 = -16 \text{ ps}^2/\text{km}$) is close to that at 1550 nm ($\beta_2 = -17 \text{ ps}^2/\text{km}$), as a result of the different FOD values at 1200 nm ($\beta_4 = 2.6 \times 10^{-4} \text{ ps}^4/\text{km}$) and 1500 nm ($\beta_4 = 1.8 \times 10^{-3} \text{ ps}^4/\text{km}$), the 30-dB bandwidth with a 1200-nm pump is 1.8 times broader than that with a 1550 nm pump. Our results show that, while low anomalous GVD is a necessary requirement for broadband combs, small FOD is also critical to further extend the bandwidth.

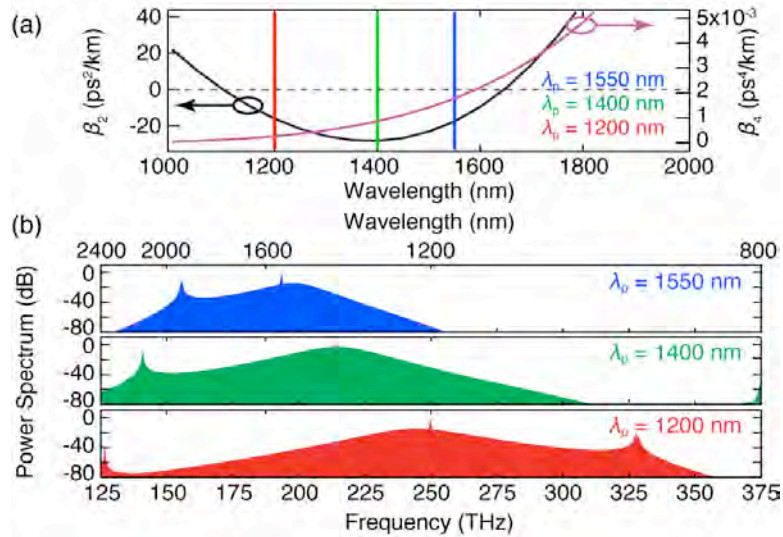


Figure 4. (a) Simulated GVD and FOD for 690×1900 nm Si₃N₄ waveguide. (b) Simulated comb spectra for pump wavelengths of 1550 nm, 1400 nm, and 1200 nm.

In addition, we observe dispersive wave (DW) formation at the edges of the comb spectra [Fig. 4(b)]. Recent studies have investigated the role of third-order dispersion (TOD) and FOD on DW formation [25,27]. The wavelength for DW formation can be predicted by phase-matching conditions between the cavity soliton and the DW wave across a ZGVD point [28]. While TOD and FOD contribute to DW generation, the group velocity of the soliton and the DW, along with the higher-order dispersion terms must be taken into account to accurately predict the spectral position for DW generation.

4. Self-Organization in Soliton Modelocked Parametric Frequency Combs

A large collection of coupled oscillators with slightly different natural frequencies can undergo a transition to a phase-locked state with identical frequencies. This phenomenon appears in many systems spanning biology, chemistry, neuroscience, and physics [29,30]. Examples include power grid networks, neural networks, chemical oscillators, and arrays of Josephson junctions and semiconductor lasers [31,32,33,34,35]. Self-organization in such systems has been modeled by the Kuramoto model, which describes the time-evolution of the phase $\phi_p(t)$ of an oscillator p as an interaction between its natural frequency ω_p and its coupling to the phases of all the other oscillators. The governing equations are $\dot{\phi}_p = \omega_p + \kappa \sum_m^N \sin(\phi_m - \phi_p)$, where κ is the coupling strength [30]. This model can be recast in an order-parameter formulation, where an average phase and a coherence $R(t)$ are defined via $R(t)e^{i\psi} = \frac{1}{N} \sum_m^N e^{i\phi_m}$. Then the Kuramoto model becomes $\dot{\phi}_p = \omega_p + \kappa R(t) \sin(\psi - \phi_p)$. Viewed this way, ϕ_p is no longer coupled to every individual oscillator's phase, but only to the average phase ψ . Moreover the effective strength of the coupling is proportional to the coherence R . This proportionality between coupling and coherence creates a positive feedback which, for a sufficiently large κ , gives rise to an abrupt transition in which a macroscopic fraction of the oscillators' frequencies spontaneously synchronize.

In optics an alternative form of phase locking can occur in lasers and parametric oscillators between a large collection of cavity modes with nearly equidistant frequency separations. In these systems the nearest neighbor spacing across the modes varies due to dispersion within the cavity. In the presence of nonlinearity within the cavity, the system can spontaneously mode-lock such that the frequency spacings between the oscillating modes become identical (Fig. 1c,d). Although Kerr-based parametric frequency combs have been suggested as the most fundamental example of self-organization in nonlinear optics [36,37], no direct connection has been made to the concepts of synchronization and self-organization. We find that phase equations derived from the Lugiato-Lefever equation (LLE) display self organization features akin to the Kuramoto model, including the existence of meaningful order parameters and coherence-coupling feedback that describes the soliton formation process [38]. These equations predict that the pump phase is offset from the rest of the modal phase profile in the soliton state. Additionally our analysis predicts that phase anti-symmetrization, where the phase profile becomes anti-symmetric about the pump phase, occurs before phase synchronization and soliton formation can occur.

Using the LL equation and employing a slowly varying envelope approximation for the total intra-cavity field and normalized dispersion coefficients $\xi_k = (2\pi v_g/L)^k v_g \beta_k$, we derive the following general dynamical phase equation, with time dependency of the phases made implicit:

$$\dot{\phi}_p = \frac{\xi_2}{2} p^2 + \frac{\xi_3}{3} p^3 - \Gamma \sum_{l,m,n=-N/2}^{N/2} A_{mp}^{ln} \cos(\phi_l - \phi_m + \phi_n - \phi_p) \quad (8)$$

where $\Gamma = \gamma L/t_R$ and $A_{mp}^{ln} = A_l A_m A_n / A_p$. This equation has functional similarities to the Kuramoto model wherein each optical mode can be considered an individual oscillator. The spread in natural frequencies of the oscillators is represented by the second- and third-order dispersion terms in the right-hand side, while the nonlinear term gives rise to the coupling among oscillators in the last term in the right-hand side. In the absence of a strong pump mode, this equation has no stable solutions. We further simplify this equation by keeping only terms that correspond to the pump-degenerate (PD) FWM processes, where two pump photons are annihilated to create a photon pair, and the pump-nondegenerate (PND) FWM processes, where one pump photon and one comb photon are annihilated to create two photons. From this approximation, we obtain a pair of equations that correspond to the phase average $\bar{\phi}_p = (\phi_p + \phi_{-p})/2$ and difference $\theta_p = (\phi_p - \phi_{-p})/2p$ for pairs of modes symmetric about the pump mode. We term the following the parametric synchronization equations (PSE):

$$\dot{\bar{\phi}}_p = \frac{\xi_2}{2} p^2 - 2\Gamma\eta^2 A_C^2 \cos[2(\phi_0 - \bar{\phi}_p)] - \Gamma\eta A_C^2 N R(t) \cos(\phi_0 - \bar{\phi}_p) \cos[p(\theta_p - \theta_o)], \quad (9)$$

$$\dot{\theta}_p = \frac{\xi_3}{3} p^2 - \frac{2\Gamma\eta A_C^2 N}{p} R(t) \sin(\phi_0 - \bar{\phi}_p) \sin[p(\theta_p - \theta_o)], \quad (10)$$

where η is the ratio between a pump and comb mode, $A_C = A_0/\eta$ is the amplitude of the comb modes, ϕ_0 is the pump phase which is fixed and N is the total number of comb modes in the system. The phase average equation describes the symmetric behavior of the system while the phase-difference equation describes its anti-symmetric behavior. The pump-nondegenerate processes have both symmetric and anti-symmetric contributions and appear as the last terms in the phase-average and phase difference equations. $R(t) = \frac{2}{N} \left| \sum_{m=1}^{N/2} e^{im(\theta_m - \theta_o)} \right|$ and

$\theta_o(t) = \frac{8}{N^2} \sum_{m=1}^{N/2} m\theta_m$ represent the order parameters of the system. Here θ_o is the normalized average phase difference. It serves the same role as the average phase ψ in the Kuramoto model.

One of the key predictions of the PSE is that the system evolves into a state in which the pump phase is offset from the rest of the phase profile. This offset arises from the cosinusoidal dependence of the PD term; in order for this term to act as a restoring force on the phase average as in the Kuramoto model, it must have a sinusoidal dependence on the phase averages. We compare in detail the synchronized spectral phase profiles in Fig. 5. Both systems stabilize to a broadband phase-locked state with an offset of the pump phase from the rest of the phase profile. Due to the factor of 2 in the argument of the PD term, this offset should be $0 < \phi_{\text{offset}} < \pi/2$ and centered at $\pi/4$ in order for the cosine to have a significant sine-like contribution. Both the PSE

and the LLE predict pump phase offsets within these bounds. The LLE system has a slightly larger pump phase offset due to self-phase and pump-induced cross-phase modulation effects that were not accounted for in the PSE. This is, to our knowledge, the first theoretical prediction and explanation of the origin of the pump phase offset of the soliton-modelocked states in a parametric frequency comb. We confirm in Fig. 5(c,d insets) that the broadband phase-locked state results in a solitary pulse in the time domain. The exact pulse shape for the PSE is not quantitatively meaningful since all the modes have equal amplitude resulting in a Sinc-like pulse without a CW background.

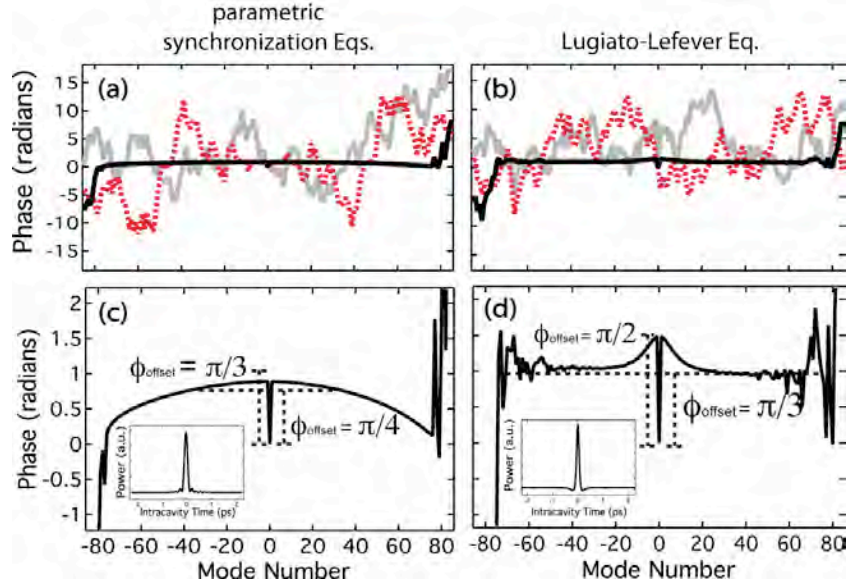


Figure 5. Three stages of evolution of the phase profile of the intra-cavity field as predicted by (a) the parametric synchronization equations (PSE) and (b) the Lugiato-Lefever equations (LLE): The grey curves represent the initial random phase profile. The red-dotted curves show the phase evolution after 370 (PSE), 308 (LLE) round trips; the phase profiles in both models illustrate the anti-symmetrization of the spectral phase due to the pump degenerate FWM processes. The black curves show the final phase profile after 3394 (both) round trips in which the phases have become completely synchronized, which is a result of the pump non-degenerate terms. In addition, a slight offset of the phase of the pump from the phases of the other cavity modes is observed. (c,d) The final spectral phase profiles of the PSE and LLE systems showing deviations from a pure linear profile, including the pump phase offsets. (insets) Temporal pulse shapes of the PSE and LLE.

5. Mode Coupling in Microresonators

The microresonator resonances can in principle be precisely calculated using the dispersion of the resonating modes and the resonator length. However, modal coupling between different types of modes can significantly alter the shape and position of their resonances. Mode splitting occurs for strong coupling [39], and coupling between whole families of modes results in avoided crossings [40,41,42,43,44,45]. Avoided crossings occur in resonators when two distinct, frequency-degenerate modes are coupled and form new eigenmodes. The frequencies of these eigenmodes are no longer degenerate with a splitting proportional to the coupling strength resulting in the absence of a crossing of the eigenmode resonances. In microresonators this behavior can lead to dramatic localized changes in the effective dispersion near these crossing points, which in general affects any parametric interaction that relies on precise frequency matching of different resonances. In particular it can play an important role in the formation of parametric frequency combs [41,42,43,44,45,46,47,48]. In the context of frequency comb generation, only modal interactions between different families of spatial modes have been considered thus far. However, in dielectric waveguides, even when the waveguide is 'single mode', there are typically at least two guided fundamental modes, the fundamental quasi transverse electric (TE_{00}) and the fundamental quasi-transverse magnetic (TM_{00}) mode, which correspond approximately to the polarization of light in the waveguide. Since such a mode interaction can even occur in single-mode waveguides, it is more universal than other forms of modal interactions (i.e., between higher-order spatial modes). The physical origin and strength of the modal coupling between the TE_{00} and TM_{00} modes are based on different parameters of the ring resonator such as its radius of curvature, waveguide cross-section, and side-wall angle [49,50]. While in most cases the polarization properties follow from the corresponding straight-waveguide characteristics [51], microresonators with smaller bend radii and larger side-wall angles typically will exhibit greater modal coupling.

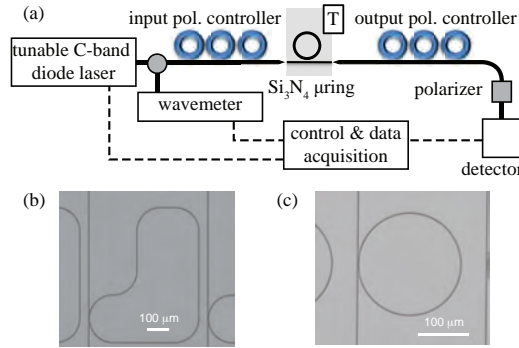


Figure 6. (a) Schematic of the setup used for observing and characterizing polarization mode coupling in microresonators on a temperature stabilized (T) silicon chip. (b),(c) SEM images of the microresonators and the coupling regions with the bus waveguides for (b) the 1.8-mm-long microresonator and (c) a 100- μ m radius ring resonator.

Our experimental setup for investigating polarization mode coupling is depicted in Fig. 6. We probe the resonators with two different external-cavity diode lasers covering a total tuning range between 1450 nm and 1640 nm. Lensed fibers are used to couple into and out of the bus waveguide with inverted tapers for mode-matching. The polarization of the input and output light

is controlled and analyzed with standard fiber-based polarization controllers and a polarization beam splitter, and the output power is monitored with a sensitive photodiode. We use a temperature controller with a Peltier element on the chip holder to stabilize and tune the Si_3N_4 microring resonators under investigation. To overcome the limited precision of our tunable lasers, we use an automated stepped scanning and fitting routine supplemented by calibrating each resonance position with a high-precision wavemeter. We find that this method leads to an average precision better than 50 MHz.

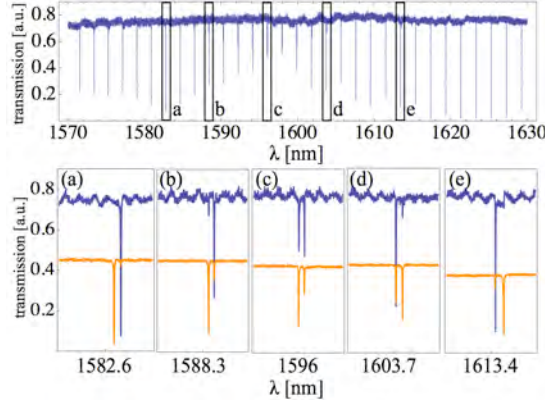


Figure 7. Optical transmission for TM_{00} polarized light and selected resonances (a) – (e) in detail for TM_{00} (blue) and TE_{00} (orange). The appearance of the TE_{00} resonances for TM_{00} polarized input (and vice versa) and their behavior indicate an avoided crossing near 1595 nm.

We first investigate polarization mode coupling in two Si_3N_4 microrings with 725×1100 nm and 725×900 nm waveguide cross-sections (effective refractive index of 1.7 for both), $100\text{-}\mu\text{m}$ radii and 10° side-wall angles [52]. The transmission measurement for TM_{00} input light for the first microring (Fig. 7) yields sharp and deep resonances due to nearly critical coupling between the bus waveguide and the resonator. Near 1595 nm a second sharp resonance, which we associate with the TE_{00} mode, appears on the right side of the main TM_{00} resonance and becomes deeper until both show the same extinction. The main resonance then experiences an adiabatic crossover and the secondary resonance (now on the left side) slowly disappears. We attribute this behavior to an avoided crossing at 1595 nm associated with a strong modal interaction between the TE_{00} and TM_{00} modes.

We further investigate the effects of both polarization and higher-order mode crossings on comb generation by directly comparing the comb spectra generated in microring resonators with a measurement of its mode-crossings (Fig. 8). The combs are generated by strongly pumping a single resonance at 1540 nm. We investigate a microring resonator with a waveguide cross-section of 725×1650 nm² (effective refractive index of 1.8), a $100\text{-}\mu\text{m}$ radius, and a 10° side-wall angle [Fig. 8(a)]. We observe a polarization mode-crossing near 1580 nm with a splitting at the avoided crossing of 2.2 GHz, which greatly exceeds the intrinsic loss rate of the resonator. This polarization mode crossing manifests as a reduction in the mode intensity in the generated comb spectrum. In addition, there exists an anomaly in the FSR at 1550 nm, which can be attributed to a mode crossing with a higher-order spatial mode, and we observe a similar corresponding feature in the comb spectrum. Furthermore, we observe suppressed comb generation when pumping near one of the higher order mode crossings which we attribute to the large change in

the effective dispersion. Since this effect can be disadvantageous for applications related to frequency comb generation, it needs to be taken into account in the optimal device design. Moreover, we investigate the effects of mode crossings on comb generation in an 80-GHz FSR microresonator with a waveguide cross-section of $725 \times 1700 \text{ nm}^2$ (effective refractive index of 1.8), a 1.8-mm length, and a 10° side-wall angle close [Fig. 8(b)]. For this microresonator our measurements reveal three polarization mode crossings and a number of higher-order mode crossings that affect the comb spectrum generated from this resonator.

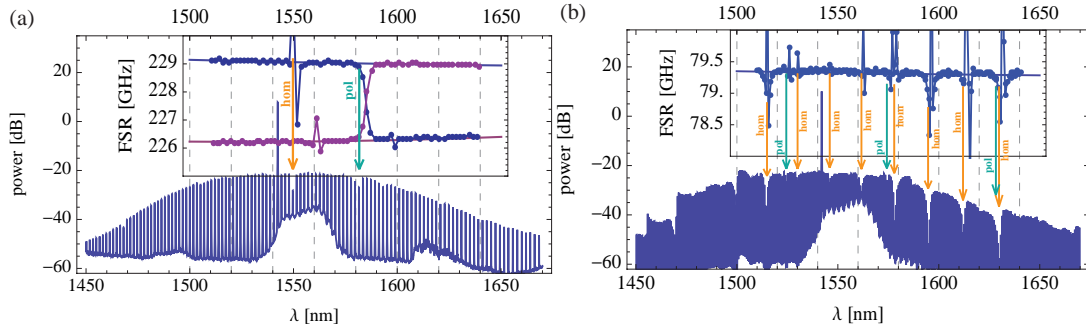


Figure 8. Generated comb spectra in Si_3N_4 microresonators. Insets show the measured FSR's with the (upper) blue branch being for the TE₀₀ mode and revealing the mode crossings. (a) Results for a $725 \times 1650 \text{ nm}$ cross-section, 100- μm radius microring. A polarization mode crossing (pol) occurs near 1580 nm with a corresponding feature (indicated by an arrow) in the comb spectrum. A second anomaly in the FSR's near 1550 nm due to a mode crossing with a higher-order spatial mode (hom) also produced a corresponding feature in the spectrum. (b) Results for a $725 \times 1700 \text{ nm}$ cross-section 1.8-mm length microresonator. A number of polarization and higher order mode crossings affect the generated comb spectrum.

We identify different strategies that could minimize the disruptive effects of mode-crossings (polarization and higher-order mode) on frequency comb generation. In general, mode-crossings are especially disruptive when they appear directly at the pump wavelength or when they line up symmetrically with respect to the pump since they will then simultaneously affect both the signal and idler resonances. Since the position of any mode-crossing depends sensitively on the exact length of the microresonators, slight variations in the design of the resonator lengths can be used to circumvent both scenarios. In addition, if the target application allows it, increasing the FSR will reduce the frequency at which mode-crossings will occur. Another approach for reducing mode-crossing disruptions would be to minimize the modal interactions altogether, which may be achieved by optimizing the microresonator design and fabrication, including larger bend radii or smaller side-wall angles. Furthermore, we have observed experimentally that higher-order mode-crossing are suppressed for the narrower and thus more symmetric cross-section resonators as compared to the wider, more asymmetric cross-section resonators. This indicates that the aspect ratio can be used as an additional parameter for controlling mode-crossing effects.

6. Tunable Frequency Combs using Dual-Microring Resonators

Tuning the coupling between the bus waveguide and resonator is challenging since in standard passive monolithically-integrated structures, the coupling gap is fixed by design and cannot be changed after fabrication. Demonstrations of tunable comb generation have included resonance frequency tunability, which enables control over the operating wavelength. Such tuning has been achieved during comb generation via both thermal and electro-optic means [6,53,54]. Coupling gap tunability enables greater control over the comb generation process, allowing for optimization of comb efficiency [55]. Coupling tunability has been demonstrated in integrated silicon devices using a Mach-Zehnder interferometer (MZI) coupler [56,57,58]. However, the coupling produced by this MZI structure inherently has a sinusoidal wavelength dependence, which can be detrimental to broadband comb generation. Coupling gap tunability can occur in suspended microtoroid and wedge resonator structures, since the devices are operated using suspended tapered fibers [6]; however, this approach requires highly stable fiber positioning with accuracy on the scale of tens of nanometers in order to achieve controllable tuning. We show a dual-cavity coupled microresonator structure in which tuning one microring resonance frequency induces a change in the overall cavity coupling condition, as evident in the transmission extinction ratio [59].

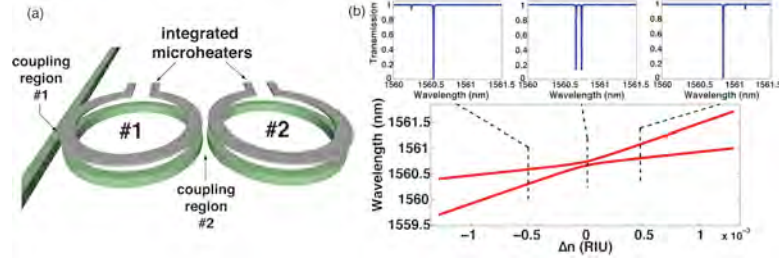


Figure 9. (a) Schematic of dual-cavity coupled microring resonator with integrated microheaters (b) Simulated mode anti-crossing curve as a function of effective mode index detuning between the two microrings. Ring #2 is tuned while ring #1 is kept constant. Insets above are simulated transmission spectra showing varying extinction across the anti-crossing.

Our structure consists of two identical microring resonators evanescently coupled to each other, with one ring coupled to a bus waveguide [Fig. 9(a)]. Due to the evanescent coupling, the two resonant cavity modes hybridize to form a coupled eigenmodes system, in which two superposition eigenmodes (“supermodes”) are formed: a symmetric (s) and an anti-symmetric (as) mode. These two new eigenmodes exhibit modified resonant frequencies, according to:

$$\omega_{s,as} = \omega_{avg} \pm \sqrt{\frac{\Delta\omega^2}{4} + \kappa_\omega^2} \quad (11)$$

in which ω_{avg} is the average of the individual cavity resonance frequencies, $\Delta\omega$ is the difference between the individual cavity resonances (cavity detuning), and κ_ω is the inter-ring temporal coupling rate. If the cavities are degenerate ($\Delta\omega = 0$), the supermode resonances are split apart from the isolated cavity resonance frequency by $\pm\kappa_\omega$. When the inter-ring coupling rate exceeds the individual cavity decay rate, distinct doublet resonances form at each cavity free spectral

range (FSR). As the detuning between the two cavities is varied, a characteristic anticrossing shape is formed, as in Fig. 9(b). At zero detuning, light resonantly couples between the two rings, resulting in an equal distribution of light in both cavities [Fig. 9(b), middle inset], and thus equal extinction in both doublet resonances. However, as the cavity detuning increases, the distribution of light becomes unequal as the resonant coupling between cavities becomes less efficient. Far from zero detuning, the modes are less hybridized, and most of the light in each of the doublet resonances is concentrated in only one ring or the other [Fig. 9(b), left/right insets]. The change in detuning also causes the effective cavity length to change, which alters the balance between the round-trip loss and the bus-waveguide coupling. This modifies the loaded- Q . The intrinsic- Q remains unchanged, as long as both cavities have the same loss rate. Figure 9(b) shows the simulated doublet resonance shape for three detuning positions along the anti-crossing curve, showing the strong asymmetry in extinction away from zero-detuning.

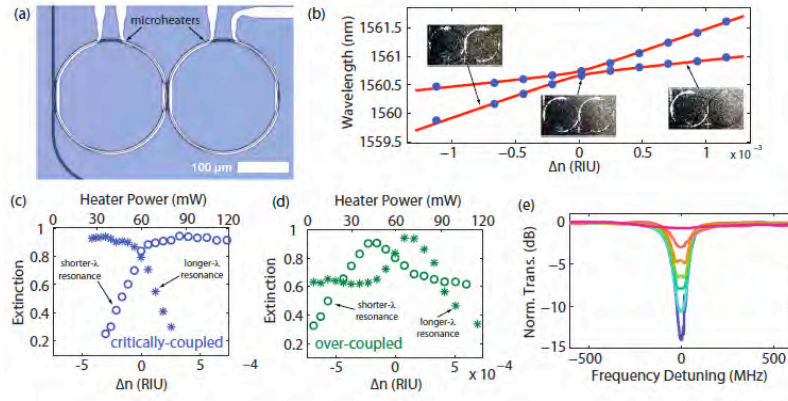


Figure 10. (a) Micrograph of fabricated dual-cavity device with integrated platinum microheaters. (b) Measured (blue points) mode anti-crossing curves with theoretical curve fit (red line). Ring #2 is tuned while ring #1 is kept fixed. The inset infrared micrographs show spatial light distribution among the two rings for 3 different positions along anti-crossing. (c) Experimental measurement of extinction vs. detuning for a critically-coupled device and (d) for an over-coupled device. Ring #2 is detuned while ring #1 is kept fixed. (e) Experimental measurement of extinction tuning at a fixed wavelength by using heater #1 for compensation. As heater #2 is increased, heater #1 is decreased in order to keep the resonance wavelength fixed.

Our fabricated devices consist of coupled high- Q Si_3N_4 microresonators with tunable extinction ratio via integrated microheaters. We fabricate a dual coupled microresonator in Si_3N_4 with cross-sectional dimensions 950×1400 nm. Our fabricated devices have an intrinsic Q -factor of approximately 2×10^6 , and radii of $115 \mu\text{m}$ as well as $75 \mu\text{m}$, yielding devices with FSR's of 200 GHz and 500 GHz, respectively. This cross-section yields anomalous GVD ($\beta_2 = -180 \text{ ps}^2/\text{km}$) at our pump wavelength of 1560 nm critical to ensure phase matching for parametric comb generation [60]. We do not observe a decrease in intrinsic- Q compared to equivalent single-ring devices; this can enable equivalent comb performance in the dual-ring device. Above the waveguide cladding, we fabricate integrated microheaters by sputtering platinum and using a lift-off approach, yielding a cross-section of 100 nm tall by 6 mm wide. We position the heaters 1.9 mm above the waveguide to ensure negligible optical loss while maintaining close proximity for efficient heat delivery. These heaters yield an efficiency of $1.35 \times 10^{-5} \text{ RIU/mW}$. We can

control the heater power to within 7 mW, resulting in a resonance wavelength accuracy of 7 MHz, which is well below the cavity linewidth.

A micrograph of the 200 GHz FSR device is shown in Fig. 10(a). Using the integrated microheaters, we first tune ring #2 while keeping ring #1 constant. In order to achieve blue detuning ($\Delta n < 0$), we bias heater #1 above room temperature. The blue data points in Fig. 10(b) are measured resonance positions as the heater on ring #2 is tuned. The red line in Fig. 10(b) is a curve fit based on Eq. (11), with an additional parameter included to account for thermal cross-talk between the two rings. In Figs. 10(c) and (d), we plot the measured extinction as a function of detuning for a critically-coupled device and an over-coupled device, respectively. Figure 10(e) shows our ability to compensate for the overall wavelength shift as the extinction is thermally tuned. By tuning both heaters independently for each ring, we are able to compensate for this wavelength shift, and demonstrate 13.3 dB of tuning of the resonance extinction, from 0.7 dB to 14 dB. Since we can keep the resonance in place as the extinction is tuned, this device is useful for real-world applications involving single-frequency lasers.

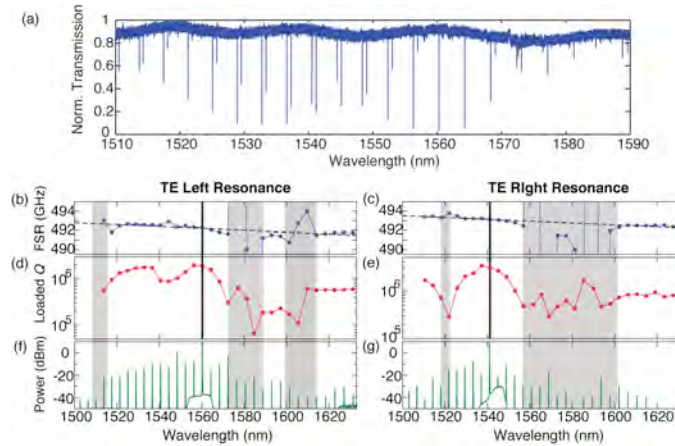


Figure 11. (a) Transmission measurement of 500 GHz FSR dual-coupled microring resonator. Measured FSR is shown for (b) lower wavelength resonance and (c) higher wavelength resonance. The corresponding loaded Q is shown for (d) lower and (e) higher wavelength resonance. The generated comb is pumped at (f) 1560 nm on a left resonance and (g) 1540 nm on a right resonance, indicated by solid black vertical lines. The shaded region indicates locations of mode-crossings that cause degradation of the comb line power.

The wide tunability of our device allows us to overcome mode-crossings resulting from strong coupling between different transverse spatial modes – a major challenge for comb generation. When mode-crossings occur, one expects the FSR to deviate strongly from the expected value, accompanied by a reduction in the Q caused by the significantly enhanced losses of the higher-order modes. In order to characterize the mode-crossings in the dual-cavity structure, we measure the FSR and loaded Q of both supermodes of a 500 GHz FSR dual-cavity device. The transmission measurement of the dual-coupled microring is shown in Fig. 11(a) and the measured FSR and the loaded Q factor are shown in Figs. 11(b)–11(e). The resonance wavelengths are precisely determined using a laser-based precision measurement of the wavelength-dependent FSR, which allows for measurement of the FSR with a relative precision of 10^{-4} [52]. The measurement indicates that the presence of mode-crossings severely disrupts the

resonance frequency position. For the left resonances, we observe large higher-order mode-crossings at 1570 nm, 1585 nm, and 1610 nm, which result in significant deviations in the FSR and additional small mode-crossings at 1520 nm and 1545 nm. For the right resonances, we observe large higher-order mode-crossings at 1560 nm and 1585 nm and a small mode-crossing at 1525 nm. These regions are indicated by gray sections in Figs. 11(b)–(g). The corresponding loaded Q characterization shows that the large mode-crossings are accompanied by a significant reduction in the Q caused by the significantly enhanced losses of the higher-order modes. As a result, pumping at these wavelengths hinders the generation of a stable comb due to insufficient power enhancement in the cavity. However, as shown in Fig. 11(f) and 11(g), by ensuring that the spectral position of these mode crossings is far detuned from the pump at 1560 nm and 1540 nm for the left resonances and right resonances, respectively, we are able to generate a stable, low- comb with 1.5 W of pump power. The generated spectra show some asymmetry, largely due to the presence of the large mode-crossings. In addition to altering the spectral position of the resonance, these mode-crossings reduce the cavity enhancement and subsequently restrict the comb bandwidth. We demonstrate that this device can be used to avoid mode-crossings by dynamically tuning the position of a mode-crossing. The ability to dynamically control the position of mode-crossings is vital particularly for many applications that cannot rely on the tuning of the pump source. Beginning with an as-fabricated 200 GHz FSR dual-cavity device with 100 mW of heating on ring #1 [Fig. 12, blue curve], we observe a mode-crossing at 1548 nm, indicated by a local decrease in extinction for a single FSR resonance. When we sweep the resonance of ring #2 by 0.4 nm (heater power from 0 to 40 mW), we observe that the mode-crossing shifts across the spectrum by over 3 nm (2 FSR's), which is almost an order of magnitude larger than the ring resonance shift. Therefore, we can tune the mode-crossing with high-efficiency. This high tuning efficiency is due to the anti-crossing behavior of the dual cavity structure. This novel degree of freedom can be used for comb generation optimization.

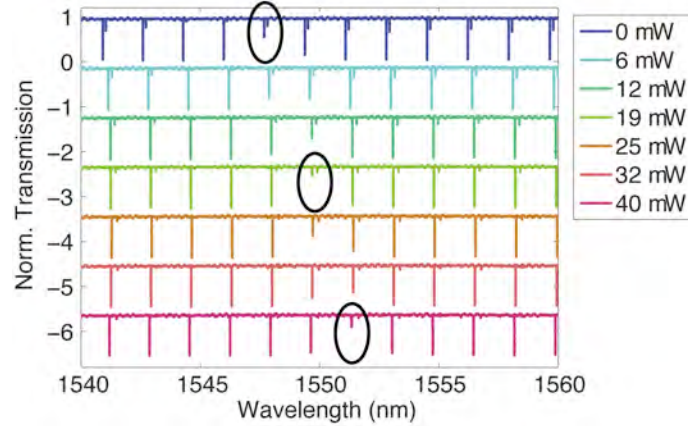


Figure 12. Demonstration of mode-crossing tenability using a 200 GHz FSR dual-cavity device. Ring #1 is heated with 100 mW and ring #2 is swept with heater power indicated in the legend. A mode-crossing (circled) is tuned across two FSR's while the overall position of the desired resonances shifts only 0.4 nm.

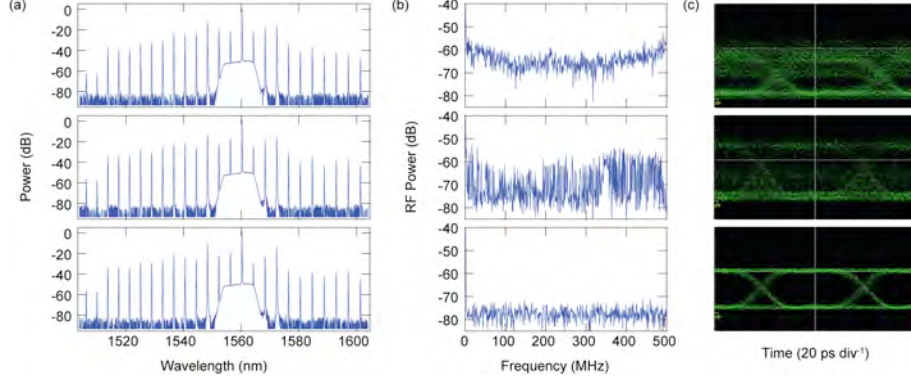


Figure 13. Comb generation dynamics for 500 GHz FSR microresonator as pump wavelength is tuned into resonance (top to bottom). Plot shows (a) optical spectra (b) RF spectra, and (c) eye diagram of single comb line that is filtered and modulated with a 10 Gb/s PRBS.

Furthermore, for the generated comb to be used as a multiple wavelength WDM source, low RF amplitude noise is required. We investigate the comb generation dynamics and the properties, in particular, to determine the stability of a comb line. We pump the resonator at 1560 nm for comb generation. To monitor the comb generation dynamics, we measure the optical and RF spectra, as well as the eye diagram through modulation of a single comb line. For the eye diagram, we use a 1 nm tunable filter to pick-off a single comb line which is modulated with a $2^{31}-1$ non-return-to-zero pseudo-random bit sequence (NRZ PRBS) at 10 Gb/s and sent to a high-speed sampling oscilloscope for characterization. Figure 13(a)–(c) shows the measured optical spectra, RF spectra, and the eye diagram, respectively, as the pump wavelength is tuned into resonance (top to bottom). While the optical spectra show no significant changes, the RF spectra show that the comb undergoes a transition to a low RF amplitude noise state, similar to behavior observed previously [11]. Furthermore the eye diagram illustrates the behavior of the comb at a single resonance. In the high-noise state (top, middle), the eye shows poor signal-to-noise and significant distortion, which can be attributed to the fast intensity fluctuations of multiple comb lines within the single resonance through various FWM processes. As the pump is tuned further, the signal-to-noise further degrades to the point where the eye is completely closed, which corresponds to comb instability from chaotic-like behavior [16]. Once the comb transitions to the low phase noise state, the eye diagram shows good signal-to-noise. Our results indicate that, even with mode-crossings in close proximity in wavelength, it is possible to generate a stable, low-noise comb suitable as a multiple wavelength source for WDM applications.

7. Microresonator-Based Comb Generation Without an External Laser Source

Frequency comb generation in microresonator platforms requires tuning an external, single-frequency, continuous-wave (cw) laser into a resonance of the microresonator. As the pump power is coupled into the microresonator, thermal effects shift the resonance to higher wavelengths, creating a soft thermal lock between the cavity resonance and the pump laser [61]. When the intracavity power exceeds the threshold for parametric oscillation, cascaded four-wave mixing and higher-order four-wave mixing processes occur, resulting in comb generation. Fluctuations in the frequency or power of the pump laser can detune the pump out of the cavity resonance, which disrupts comb generation. These limitations can be overcome using a drop-port of the microresonator as shown by Peccianti *et al.* [62,63] with a hydrex microring imbedded in a fiber cavity pumped with an erbium-doped fiber amplifier (EDFA). Through filter-driven four-wave mixing, they demonstrate a high-repetition-rate pulse source with a 60-nm bandwidth and a 200-GHz repetition rate. In this drop-port configuration the microresonator acts as a filter, seeding the EDFA with wavelengths that correspond to resonances of the microresonator, similar to the recent work done by Cholan, *et al.* [64] for realization of a multiple wavelength source.

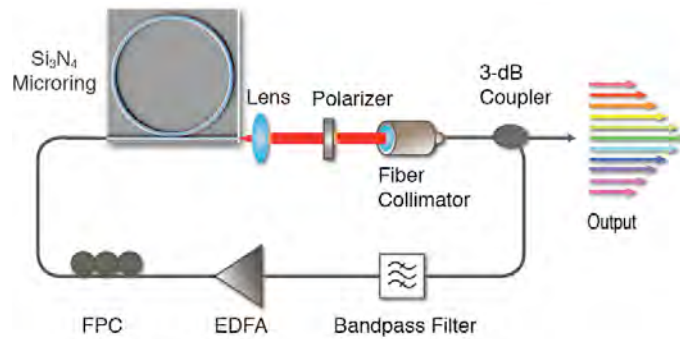


Figure 14. Experimental setup for comb generation. The system is based on a dual-cavity design consisting of the silicon-nitride microresonator and an external fiber cavity.

We explore a dual-cavity architecture where a single bus waveguide (through-port), which forms part of the external fiber cavity, is coupled to the microresonator (Fig. 14). Amplified spontaneous emission (ASE) from an EDFA is coupled into a silicon-nitride microresonator. A fiber polarization controller (FPC) allows for adjustment of the polarization of light coupled to the microresonator, which is a critical issue for cw lasing of the external fiber cavity and comb generation. A polarizer is placed at the output to select quasi-TE polarization. The dispersion of the microresonator waveguide is engineered to optimize parametric FWM gain and oscillation for the TE modes. Due to the higher density of photonic states in the microresonator as compared to the fiber cavity, preferential emission occurs at the microresonator modes resulting in lasing and parametric comb generation defined by the microresonator. Our through-port configuration is effectively analogous to microresonator-based comb generation using a cw pump laser. Additionally, since only a single bus waveguide is coupled to the microresonator, the system operates with reduced coupling losses and allows for higher power efficiency. Through the use of this dual-cavity design, we achieve broadband comb generation spanning more than 880 nm.

Key advantages of this scheme are that the system requires only a narrow-band optical amplifier, as opposed to a stabilized single-frequency laser, and that it eliminates the need to pump at and tune to a resonance wavelength which eliminates disruptions to comb generation due to pump frequency fluctuations which can shift the pump out of resonance.

We apply the dual-cavity design to produce a broad comb spectra using a 230-GHz free spectral range (FSR) microresonator with a waveguide cross section of 725×1600 nm to provide a broad region of anomalous dispersion which yields a comb spectrum spanning 880 nm (90 THz) with over 390 comb lines when pumped with 2.17 W of EDFA power [Fig. 15(a)]. For a microresonator with an 80-GHz FSR and 725×1700 nm cross section a bandwidth of 730 nm (78 THz) [Fig. 15(b)] is achieved with 2 W of EDFA power.

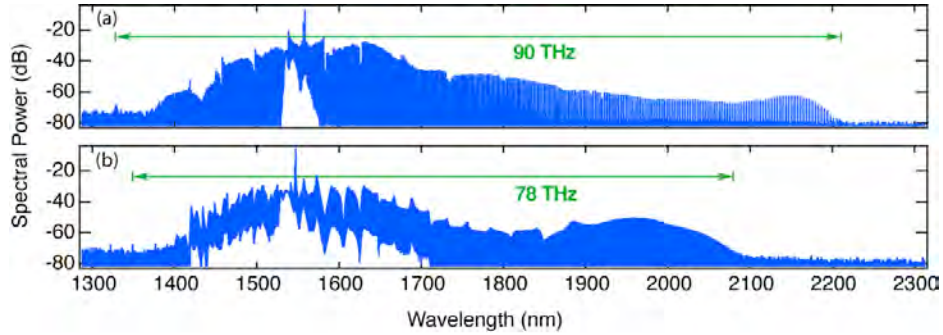


Figure 15. Parametric frequency comb spectra generated from silicon-nitride microresonators with FSR's of (a) 230-GHz and (b) 80-GHz.

In order to understand the spectral properties of our dual-comb system, we perform simultaneous RF and optical spectral measurements of the dual-cavity output. We utilize the dual-cavity configuration with the bandpass filter removed from the external fiber cavity. By adjusting the polarization, we allow the external fiber cavity to lase without interaction with the resonator [see Fig. 16(a)]. The output from the bus waveguide is detected with a 12.5-GHz photodiode, and the resulting RF signal is amplified with a 0.1 – 500-MHz low-noise amplifier and measured using an RF spectrum analyzer. The detected RF beatnote is 5 MHz [Fig. 16(c)], which corresponds to beating of the external cavity modes since the 1-GHz linewidth of the microresonator mode supports multiple modes of the external cavity. The inset in Fig. 20(c) further illustrates this multi-mode behavior as the RF noise is present out to 2 GHz. Next, the polarization in the bus waveguide is rotated to quasi-TE for comb generation and the entire comb output is sent to the photodiode and RF amplifier for characterization. The measured optical power at the photodiode is equal to that for the case of lasing in the fiber cavity. When a state of steady comb generation is reached [Fig. 16(b)], despite the multi-mode pump, a steady state of comb generation can be reached in which the RF amplitude of the 5 MHz beatnote is reduced by 20 dB, and the beatnote linewidth broadens significantly [Fig. 16(d)]. In addition, Fig. 16(d) inset shows 220 MHz (3-dB bandwidth) of RF noise during comb generation, indicating that the number of oscillating external cavity modes is greatly reduced when comb generation occurs. We believe the system can be further improved to allow for single-mode operation by reducing the external cavity length. Additionally, we expect that complete stabilization of the comb can be achieved through FSR control of both the microresonator and external fiber cavity.

Microresonator FSR stabilization can be implemented through pump power or temperature control, while stabilization of the external fiber cavity FSR can be performed using a piezo-based delay arm.

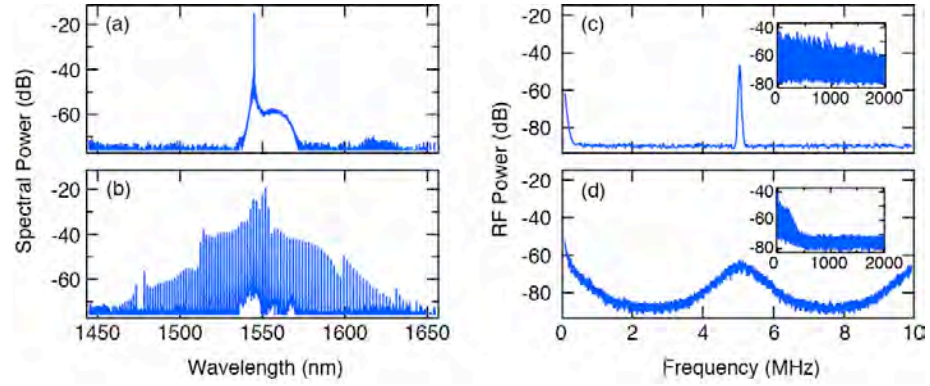


Figure 16. Optical output spectra without (a) and with (b) coupling to the microresonator and (c) and (d) are the corresponding RF spectra, respectively. The insets in (c) and (d) show the RF noise from DC to 2 GHz.

8. Frequency Comb Generation Near Visible Wavelengths

Comb generation near the visible wavelength range is of particular interest since there are several atomic absorption lines such as rubidium and cesium, to which frequency combs can be locked, providing stable frequency references for frequency metrology and optical clockwork. In addition, the 800 to 900 nm range is of interest for biological applications since it is a suitable compromise between increased scattering at shorter wavelengths and increased water absorption at longer wavelengths. The high coherence of frequency comb lines also allows for deeper tissue penetration and higher resolution imaging, particularly for optical coherence tomography [65]. Previous attempts at broadband comb generation near the visible wavelength range have resulted in combs that are either narrowband or fall below the detection noise floor well before approaching visible wavelengths. Comb generation closer to the visible wavelength range has been previously demonstrated by pumping at 1 μm [66], but the shortest wavelength to which this comb could generate was 950 nm. These combs fail to extend to shorter wavelengths since the GVD of these microresonator designs cannot adequately compensate for the stronger material dispersion at shorter wavelengths. Anomalous GVD is required for the FWM gain that produces parametric oscillation, but the increasingly strong normal GVD of the material as the wavelength approaches the absorption band edge is fundamental to most optically transparent materials.

First, we demonstrate broadband comb generation with a 1- μm pump. We engineer the dispersion of a Si_3N_4 ring resonator to overcome the stronger material dispersion at lower wavelengths, and we simulate the comb formation dynamics to ensure broadband comb generation. We use anomalous waveguide dispersion due to the high confinement of the optical mode to adequately compensate for the normal material GVD of Si_3N_4 . While previous demonstrations have also used this approach, we further optimize the dispersion of the ring resonators by simulating the comb formation dynamics for various cross sectional shapes. We simulate the comb spectrum [shown in Fig. 17(a)] using the modified LL model [16]. The microresonator has a radius of 46 μm and is pumped at 1060 nm with 1.5 W in the coupling waveguide. Our simulations indicate that the comb output exhibits stable, single-pulse modelocking behavior. Modelocking gives precisely uniform comb spacing, which is desirable for many of the metrology and clocking applications of frequency combs. Experimentally we generate a frequency comb by pumping a cavity resonance of a Si_3N_4 microring resonator with a single-frequency tunable diode laser amplified by a ytterbium-doped fiber amplifier. We use a polarizing beam cube and a half-wave plate to set the input polarization to quasi-transverse electric (TE) and a bandpass filter to reduce the amplified spontaneous emission (ASE) noise of the amplifier. In order to couple light into the chip, we focus the beam onto the nanotaper coupler of the Si_3N_4 coupling waveguide. The light then couples into a ring resonator with cross section of 690×1400 nm, coupling gap of 380 nm, and ring radius of 46 μm . We collect the output with lensed fiber and record the frequency comb spectrum on an optical spectrum analyzer while monitoring 10% of the output power on a detector. To increase the circulating power in the resonator, we tune the pump wavelength into resonance, which causes parametric oscillation and cascaded FWM to occur, resulting in comb generation.

We experimentally demonstrate a broadband frequency comb spanning 830 to 1540 nm, shown in Fig. 17(b),(c), which represents, to our knowledge, the broadest comb demonstrated near the visible wavelength range [67]. This wavelength range includes both the D1 and D2

atomic absorption lines of cesium at 895 nm and 852 nm, respectively, to which the frequency comb can be locked. This frequency comb also encompasses much of the range desired for OCT and other biological imaging applications. The demonstrated comb is generated with an amplifier power of 10 W, but this power can be drastically reduced with improved coupling efficiency and quality factor (Q). For the device demonstrated, we measure a coupling efficiency of 6dB into the chip and loaded Q of 500,000, both of which can be further improved. The Q is lower than expected due to resist polymerization issues during fabrication. Since the optical parametric oscillation threshold is inversely proportional to the square of the Q , an increase in Q will dramatically reduce the required amplifier power. These improvements will lower the required amplifier power and increase the bandwidth of the comb. Although we have not yet seen evidence of single-pulse modelocking behavior, simulations confirm that this can occur at higher powers or with the fabrication improvements mentioned above.

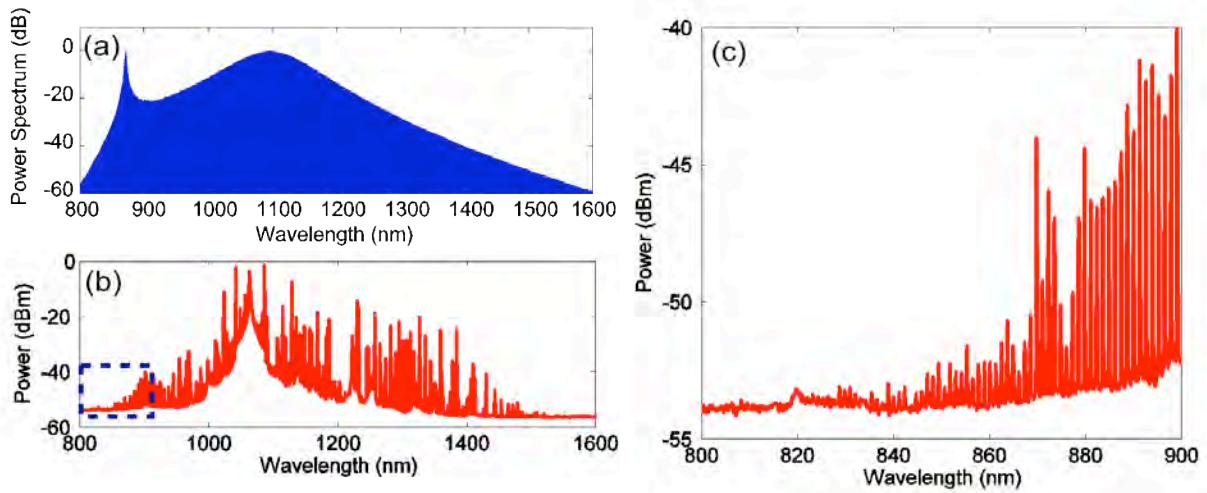


Figure 17. (a) Frequency comb simulation for 1 μ m pump. (b) Experimentally measured comb spectrum, and (c) comb lines generated at the short wavelength edge of the comb indicated in inset of (b).

Next, we circumvent the traditional challenges in achieving microcombs in the visible range and instead simultaneously employ the second- and third-order nonlinearity of silicon nitride (Si_3N_4) to generate frequency comb lines at visible wavelengths. Silicon-based materials have traditionally been limited to third-order ($\chi^{(3)}$) nonlinear interactions as they are inherently centrosymmetric in either crystalline (c-Si) or amorphous (a-Si or SiN_x) forms. Second-order nonlinear optical processes require breaking the symmetry of the material. The recent demonstrations of Si_3N_4 as a second-order nonlinear ($\chi^{(2)}$) material [68,69,70,71,72] has expanded the range of possible applications for this CMOS-compatible platform. The symmetry-breaking in these otherwise-centrosymmetric materials has been attributed to 1) high levels of strain in the waveguide material [73], 2) surface effects from waveguide-cladding interfaces, which removes the bulk symmetry of the amorphous film [68,70], and 3) embedded silicon defects or nanoclusters [71,72]. The $\chi^{(2)}$ coefficient has been estimated to be as high as 5.9 pm/V in Si_3N_4 [72]. Second-order nonlinear processes such as second-harmonic or sum-frequency generation inherently involve wide, octave-spanning frequency conversion away from the pump

frequency, as opposed to third-order processes such as FWM, which typically involve narrow conversion near the pump frequency. Here we use this wide-band attribute of $\chi^{(2)}$ nonlinearity to achieve wide frequency conversion from near-IR into visible wavelengths.

We generate a parametric frequency comb in the near-IR using $\chi^{(3)}$ and frequency- translate it into the visible range [Fig. 18(a)] using $\chi^{(2)}$ in an integrated ring resonator cavity. A single-frequency, continuous-wave (CW) pump laser in the near-IR is coupled into a high- Q Si_3N_4 ring resonator, which acts to enhance the pump power and serves as the nonlinear medium. The pump laser first undergoes $\chi^{(2)}$ second-harmonic generation (SHG), producing one line in the visible range. As the cavity circulating power increases, the pump undergoes $\chi^{(3)}$ FWM optical parametric oscillation, which produces a frequency comb in the near-IR range [Fig. 19(b)]. The comb lines then mix with the strong near-IR pump through a $\chi^{(2)}$ sum-frequency generation (SFG) process [Fig. 18(c)], which produces a set of comb lines in the visible range that are generated simultaneously with the near-IR comb. The generated comb lines therefore simultaneously address two widely different wavelength bands. Additionally, all processes are achieved in a single integrated device using a single CW laser source.

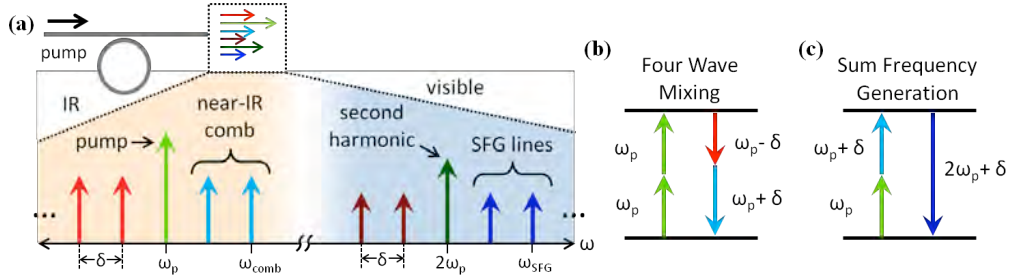


Figure 18. (a) A single near-IR pump is coupled into a microring cavity and undergoes second-harmonic generation, near-IR frequency comb generation, and sum-frequency generation to generate simultaneous near-IR and visible wavelength frequency comb lines. (b) Nonlinear photon interaction energy conservation for degenerate FWM optical parametric oscillation in the near-IR. (c) Nonlinear photon interaction energy conservation for sum-frequency generation between one pump photon and one comb line photon generating a comb line in the visible.

We engineer the waveguide dispersion to simultaneously phase-match near-IR frequency comb generation, second-harmonic generation, and sum-frequency generation. The high finesse of the Si_3N_4 cavity enhances the efficiency of nonlinear processes. The use of high-index contrast waveguides provides the ability to readily control the waveguide dispersion, and using Si_3N_4 eliminates the negative effects of free carriers and two photon absorption at the operating wavelengths [74]. Through dispersion engineering, we simultaneously satisfy the phase-matching conditions for each nonlinear process. For efficient SHG, the effective indices of the fundamental and second harmonic (SH) modes must match. This phase-matching is achieved by using a higher-order waveguide mode for the SH light, as in [68]. The third-order TE mode at twice the fundamental frequency is designed to have the same effective mode index as the fundamental TE mode of the pump. We use a finite-element mode solver to calculate effective indices of each mode by taking into consideration material dispersion, a 4° sidewall angle introduced during fabrication, and the waveguide bending radius of $104\ \mu\text{m}$. As shown in Fig. 19(a), this phase-matching condition is satisfied at a fundamental wavelength of $1540\ \text{nm}$ for a

waveguide with dimensions 700×1400 nm. This waveguide dimension is also chosen to optimize optical parametric oscillation. The phase-matching condition for optical parametric oscillation is largely dependent on group-velocity dispersion (GVD). The optimal condition for oscillation is a low level of anomalous GVD at the pump frequency [8]. This dispersion is then compensated by the $\chi^{(3)}$ nonlinear phase shift in order to achieve the proper phase-matching for degenerate FWM. As shown in Fig. 19(b), the waveguide dimensions that satisfy SHG phase-matching also exhibit a sufficiently low level of anomalous GVD for efficient parametric oscillation.

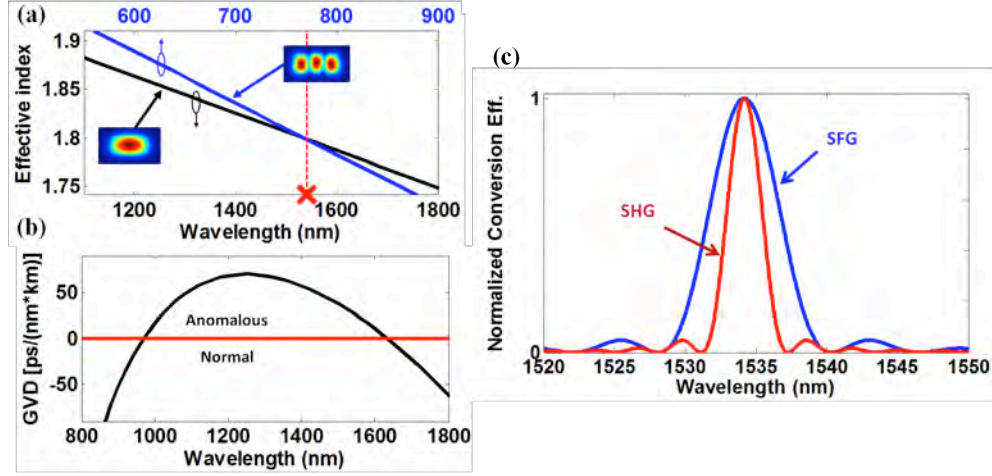


Figure 19. (a) The effective mode index dispersion of the fundamental TE mode in near IR spectral range and the third order TE mode in the visible spectral range. One can see that around the pump wavelength of 1540 nm (red X), phase-matching occurs. (b) The GVD of the fundamental TE mode shown in (a). The low level of anomalous GVD at the pump wavelength of 1540 nm allows for efficient frequency comb generation. (c) Conversion efficiency vs. wavelength for $\chi^{(2)}$ SHG and SFG processes, estimated using Eq. (12). Phase-matching bandwidth for SFG is wider than for SHG, allowing for multiple comb lines to be converted into the visible range.

Once phase-matching is ensured for both FWM and SHG processes, the final SFG process is automatically phase-matched, resulting in simultaneous phase-matching for all desired processes. The phase-matching of the SFG process involves one photon from a comb line mixing with one photon from the strong pump. Fig. 19(c) shows normalized conversion efficiency versus wavelength for SFG, which follows the same phase matching condition as SHG only with two photons allocated for the pump. The phase-matching requirement for SFG is less stringent than that of SHG, which provides the opportunity to convert a wider bandwidth of near-IR comb lines into the visible range. This bandwidth is determined primarily by the slope of the phase-mismatch Δk with respect to wavelength, which in turn is determined by the group index mismatch of the fundamental and higher-order modes. The choice of a different higher-order mode with a group index closer to that of the fundamental mode could further increase the conversion bandwidth. Overall, these three nonlinear processes are simultaneously phase-matched and are able to occur together in the same cavity structure.

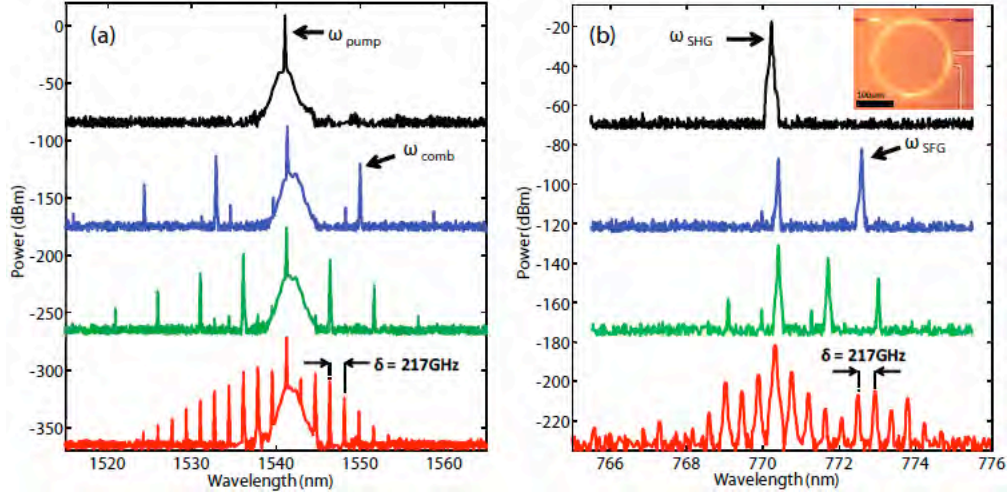


Figure 20. (a) Near-IR cw pump laser and frequency comb generation. Several different states of the frequency comb are shown. (b) Visible second-harmonic generation and frequency comb lines for corresponding spectra in (a). Inset micrograph shows the visible light generated by the device.

We measure up to 17 comb lines frequency-translated from near-IR into visible wavelengths extending from 765–775 nm. We use a Si_3N_4 ring resonator with radius 104 μm , waveguide dimensions 700×1400 nm and a coupling gap of 560 nm. The resonator has a $Q = 1.5 \times 10^6$. All nonlinear processes occur inside the resonator cavity, and are enhanced by this high Q . The pump is produced by a single-frequency tunable diode laser amplified with an erbium-doped fiber amplifier (EDFA). The amplified spontaneous emission (ASE) noise from the EDFA is filtered using a 1-nm tunable bandpass filter, and a polarization controller is used to couple to the fundamental quasi-TE mode of the waveguide using a single-mode lensed fiber. The pump is tuned into a cavity resonance near 1540 nm (Fig. 20(a), black curve). At low circulating power in the cavity, the second-harmonic is generated at the expected wavelength of 770.3 nm, as shown in the black curve of Fig. 20(b). The maximum second harmonic conversion efficiency we measure is -29 dB, in which ~1 mW of the second harmonic has been generated. As the pump is tuned into the resonance, the circulating power in the cavity builds up, which leads to the onset of near-IR frequency comb generation as well as frequency conversion of the comb lines into the visible range. A micrograph inset shows the generated visible light. Several states [75] of the generated comb are shown, with comb lines generated every 5, 3, and 1 free-spectral ranges (FSR's). In the filled-in comb state (red), we observe a visible comb bandwidth of nearly 10 nm, covering 17 FSR's. There is equal frequency spacing of 217 GHz among the near-IR comb lines and the visible comb lines. The SFG conversion efficiency is approximately -20 dB. We believe this conversion efficiency is higher than the SHG conversion of the pump due to a lack of precise pump phase-matching for this resonator. This is evident in the blue curve in Fig. 20(b) where we see that the converted comb line five FSR's away has a higher power than the second-harmonic of the pump.

9. Frequency Comb Generation in the Mid-Infrared

Silicon, due to its CMOS compatibility, wide transparency window, and high third optical nonlinearity, is an ideal platform for on-chip comb generation deep into the mid-IR. However, its linear and nonlinear losses have until now prevented the realization of a silicon microresonator-based comb source. Silicon has a wide transparency window from 1.2 μm to past 8 μm [76] and a large third-order optical nonlinearity ($n_2 = 10^{-14} \text{ cm}^2/\text{W}$ at 2.5 μm wavelength [77]), which makes it an excellent platform for mid-IR nonlinear optics. In etched silicon microresonators, quality factors have been limited by scattering losses due to roughness in the waveguide sidewalls, which is made worse by the high index contrast between waveguide core and cladding. The dominant nonlinear loss in silicon in the 2.2 – 3.3 μm region is three photon absorption (3PA) – a process where three photons are simultaneously absorbed to excite an electron-hole pair [78]. The number of photons lost directly to 3PA is small (dominated by linear waveguide losses), but the generated free-carrier (FC) population will induce significant optical losses¹⁹. Here we overcome both silicon’s high linear and nonlinear losses to demonstrate a silicon microresonator frequency comb source, and to show the fabrication techniques necessary to achieve an on-chip integrated microresonator comb source in the mid-IR.

We overcome silicon’s linear losses using a novel etchless fabrication process based on thermal oxidation to achieve a high quality factor of 590,000 in a silicon microresonator at a wavelength of 2.6 μm . The silicon waveguide is defined in an etchless manner using thermal oxidation, instead of dry etching, to form the waveguide core [79,80]. We characterize the resonator quality factor by sweeping a narrow linewidth source across the resonance, and the loaded quality factor is 220,000 and the one is 590,000, which corresponds to a propagation loss of 0.7 dB/cm. In order to enable broadband comb generation, we engineer the etchless waveguide geometry to have anomalous group velocity dispersion from 2.2 to 3 μm . To mitigate silicon’s nonlinear loss, we embed the silicon microresonator in a reverse biased positive-intrinsic-negative (PIN) doped junction to sweep out carriers generated from three-photon absorption. Significant FC’s accumulate when pumping a passive silicon waveguide with a continuous wave (cw) laser, limited only by the natural FC lifetime of the structure. Here, we counteract the carrier generation while using a cw pump by extracting the generated carriers using a PIN junction operated in reverse bias [81]. The PIN junction prevents the electrical injection of carriers into the waveguide while allowing generated free carriers to be swept out – with effective FC lifetimes demonstrated as short as 12 ps [82].

We demonstrate the generation of an optical frequency comb between 2.1 μm and 3.5 μm under reverse bias conditions (Fig. 21). We use as our source an Argos Model 2400 CW optical parametric oscillator, which is a tunable from 2500 to 3200 nm with a 100 kHz linewidth. We couple 1.2 W of optical power at 2.59 μm into a lens, which focuses the light into a silicon nanotaper on the chip. The input coupling loss is roughly 9 dB, leading to 150 mW of optical power coupled into the bus waveguide on the chip. By tuning into resonance from the short wavelength side, we achieve a soft thermal lock, where cavity heating is compensated by diffusive cooling to maintain constant power in the resonator. Once on resonance, we extract 2.7 mA of current, using 10 volts of reverse bias applied to the PIN junction. This relatively high current is an indication that three-photon absorption is significant at these power levels. We

collect the output light from the nanotaper using another lens, and couple this light to a Fourier transform infrared spectrometer (FTIR). The generated frequency comb has a uniform line spacing of 127 ± 2 GHz, well below the 7.5 GHz resolution limit of the FTIR. This corresponds well with the expected free spectral range (FSR) of the resonator.

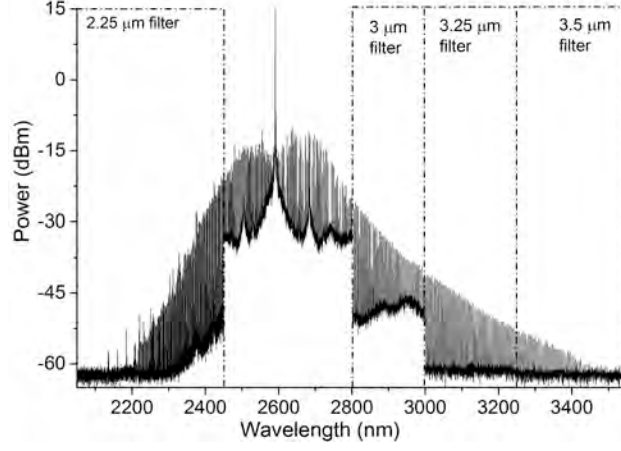


Figure 21. Broadband mid-infrared frequency comb generation from 2.1 μm to 3.5 μm in the etchless silicon microresonator. This frequency comb is generated with 150 mW of optical power in the bus waveguide, and with 10 V reverse bias applied on the PIN junction.

We investigate the role of FC absorption in silicon microresonator-based frequency combs and discuss the implications of operating in the telecom and MIR wavelength ranges. The nonlinear dynamics of microresonator-based frequency combs are complex, and simulation of the process over broad bandwidths is intensive. We apply a model based on the LL equation, but include effects of multi-photon absorption and FC effects, such that

$$\begin{aligned}
 t_R \frac{\partial E(t, \tau)}{\partial t} = & \sqrt{\kappa} E_{\text{in}} + \left[-\frac{\alpha}{2} - \frac{\kappa}{2} - i\delta_0 + iL \sum_{n \geq 2} \frac{\beta_n}{n!} \left(i \frac{\partial}{\partial \tau} \right)^n + \left(1 + \frac{i}{\omega_0} \frac{\partial}{\partial \tau} \right) i\gamma L |E(t, \tau)|^2 \right] E(t, \tau) \\
 & + \left(1 + \frac{i}{\omega_0} \frac{\partial}{\partial \tau} \right) \left[-\frac{\beta_{2PA} L}{2A_{\text{eff}}} |E(t, \tau)|^2 - \frac{\beta_{3PA} L}{3A_{\text{eff}}^2} |E(t, \tau)|^4 - \frac{\beta_{4PA} L}{4A_{\text{eff}}^3} |E(t, \tau)|^6 \right] E(t, \tau) \\
 & + \left(1 + \frac{i}{\omega_0} \frac{\partial}{\partial \tau} \right) \left[-\frac{\sigma L}{2} (1 + i\mu) N_c(t, \tau) \right] E(t, \tau)
 \end{aligned} \tag{12}$$

where $E(t, \tau)$ is the field within the microresonator, E_{in} is the input field at frequency ω_0 , t and τ correspond to the “slow” and “fast” time variables, respectively, t_R is the round-trip time, κ is the power transmission coefficient, α is the round-trip loss, δ_0 is the cavity detuning, L is the cavity length, β_k is the k -th order dispersion coefficient, γ is the nonlinear parameter, β_{2PA} , β_{3PA} , and β_{4PA} are the two-, three-, and four-photon absorption coefficients of silicon, respectively, A_{eff} is the effective area of the waveguide mode, and σ and μ are the FC absorption (FCA) cross section and FC dispersion (FCD) parameter, respectively [83,84]. The FC density N_c is governed by the rate equation:

$$\frac{\partial N_C(t, \tau)}{\partial \tau} = \frac{\beta_{2PA}}{2\hbar\omega_0} \frac{|E(t, \tau)|^4}{A_{eff}^2} + \frac{\beta_{3PA}}{3\hbar\omega_0} \frac{|E(t, \tau)|^6}{A_{eff}^3} + \frac{\beta_{3PA}}{3\hbar\omega_0} \frac{|E(t, \tau)|^6}{A_{eff}^3} - \frac{N_C(t, \tau)}{\tau_{eff}}, \quad (13)$$

with carrier generation rates determined by multiphoton absorption and the recombination rate determined by the effective FC lifetime τ_{eff} . Equation (16) describes the evolution of free carriers on the “fast” time scale within a round trip of the microresonator. The accumulation of free carriers over successive round trips is included in the boundary condition $N_C(t, -t_R/2) = N_C(t + \Delta t, +t_R/2)$.

We consider an oxide-clad, etchless silicon device similar to that used in the experiment pumped with 1 W at 2.4 μm , where three-photon absorption (3PA) becomes the dominant nonlinear absorption process. The spectra generated in the absence of 3PA (blue), presence of 3PA without FC (green), and presence of 3PA and FC (red) are presented in Fig. 22. We observe once again that oscillation does not occur when all the nonlinear loss terms are included. Interestingly, in contrast to the telecom frequency comb, it is evident that the limiting mechanism in this case is the FCA and not the 3PA, as simulations which include 3PA without FC effects (green) are similar to those without any nonlinear loss terms (blue). Since the rate of FC generation is intensity dependent, one approach to mitigate FCA is simply to lower the pump power and reduce the on-chip optical intensity while remaining above the threshold power for parametric oscillation. The threshold power is primarily determined by the linear losses and effective nonlinearity of the resonator and is on the order of a few mW’s for our devices. We note that the threshold power is independent of the FC lifetime in the regime presented here since oscillation is achieved at lower powers where FCA is not significant. By reducing the pump power to 10 mW, a frequency comb is generated at 2.4 μm , despite the presence of 3PA and FCA. However, this approach limits the achievable parametric bandwidth and is not conducive to generating a broadband comb.

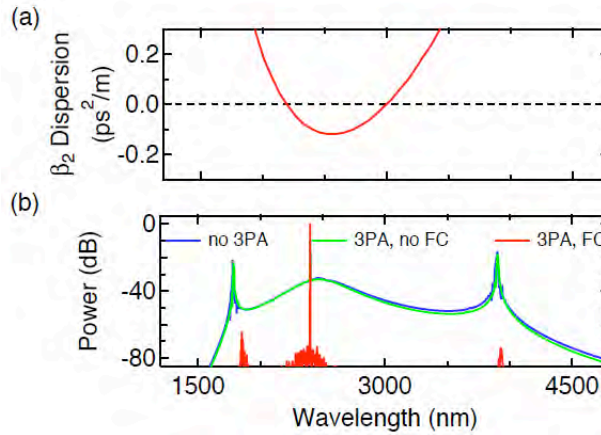


Figure 22. (a) Waveguide GVD and (b) simulated frequency comb spectra for etchless silicon microresonator engineered for the MIR range. Spectra are generated in the absence of 3PA (blue), presence of 3PA with no FC (green), and presence of 3PA and FC (red) using 1 W of pump power at 2.4 μm .

10. Supercontinuum Generation in Si-Based Nanowaveguides

Coherent supercontinuum generation (SCG) has been utilized as a phase-coherent broadband source for biological imaging and molecular detection techniques. A phase-coherent optical spectrum is also critical for applications including pulse compression [85], frequency metrology [86,87], and wavelength division multiplexing [88]. Additionally, coherent supercontinuum (SC) with an octave-spanning bandwidth is highly desirable for the detection of the carrier envelope offset frequency (f_{ceo}) of a modelocked laser through a self-referencing scheme using f - $2f$ interferometry [86,87], enabling a fully-stabilized frequency comb source. For some applications, such as dual-comb spectroscopy, where the resolution is determined by the comb spacing, the desired source repetition rate is determined by the sample that is characterized [89,90]. Thus a SC platform that can operate over a wide range of pulses energies and repetition rates is highly advantageous. Chip-based SCG offers the potential for cost-efficient, large-scale production, and more importantly, the potential for a completely integrated photonic SC source. Current CMOS-compatible chip-based SCG platforms include silicon [91,92,93], amorphous silicon [94], silica [95], high-index doped silica [96], silicon nitride [97,98,99,100,101]. Silicon-based waveguides in particular provide material compatibility with existing complementary metal-oxide-semiconductor (CMOS) fabrication technology which allows for wide scale implementation of integrated chip-scale devices. Previous demonstrations of SCG in Si_3N_4 with near-infrared [97,98,99,100] and mid-infrared [101] pump lasers have achieved octave-spanning bandwidths, but the coherence of the generated SC spectra has not been characterized.

We characterize the spectral coherence by interfering the the SC generated from a single input pulse with the spectrum generated from a previous pulse. From this measurement we find that the generated SC is highly coherent over the majority of its bandwidth and is suitable for f - $2f$ interferometry. We achieve coherent broadband SCG in a Si_3N_4 ridge waveguide through careful design of the dispersion. SCG at a specific pump wavelength is accomplished through modification of the waveguide cross section to tailor the appropriate contribution from the waveguide dispersion. The region of anomalous GVD at the pump wavelength allows for coherent SCG through soliton fission when pumping with adequately short pulses, and the two zero-GVD points allow for dispersive wave emission on either side of the pump wavelength which serves to extend the coherent bandwidth of the generated SC [17].

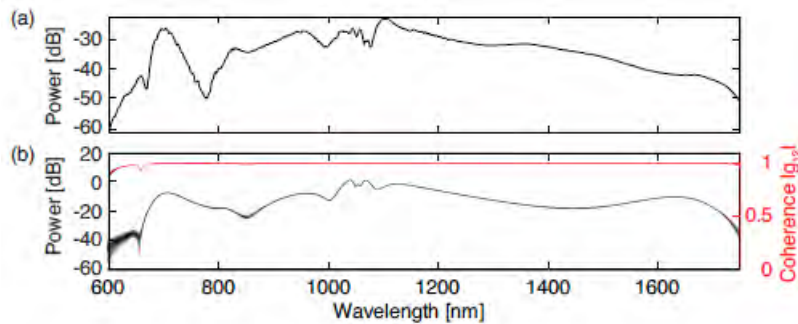


Figure 23. (a) Experimental SCG for a 7.5-mm-long waveguide with 690×900 nm cross-section and 37 pJ of coupled pulse energy. (b) Left axis: Individually simulated SC spectra and ensemble average (black) for such a waveguide. Right axis: Simulated coherence of the generated spectra is unity over the entire bandwidth.

We demonstrate SCG using a 1-GHz repetition rate SESAM-modelocked diode-pumped Yb:CALGO laser [102,103]. This laser allows for a relatively easy coherence measurement due to the short delay in the path length (30 cm) between adjacent pulses. The laser pulses have a hyperbolic secant intensity profile and a center wavelength of 1055 nm. An optical Faraday isolator is used after the laser to protect against back reflections from the waveguide facet, and a grating pair is used to compensate for the GVD introduced by the isolator. Residual GVD and higher-order dispersion result in stretching of the laser pulses from 63-fs pulses before the isolator to 91-fs pulses after the isolator and grating pair. Back reflections from the waveguide can be suppressed in subsequent designs through use of an angled waveguide facet, eliminating the need for an isolator. The setup for SCG is the same as described above. The Si₃N₄ waveguide is 7.5-mm-long with a 690×900 nm cross section. Figure 23(a) shows the SC generated with 236 pJ pulses incident on the waveguide with an 8-dB coupling loss. The measured SC is generated with 37 pJ of coupled pulse energy. We theoretically investigate the coherence of the SC spectrum by performing numerical SCG simulations using the split-step Fourier method to solve the generalized nonlinear Schrödinger equation including third-order nonlinearity, higher-order dispersion, and self-steepening. To characterize the spectral coherence, the input pulses are seeded with quantum shot noise [104], and the first-order mutual coherence function for the simulated SC is calculated based on [105]. The simulated SC of the 7.5-mm-long waveguide using 91-fs time-bandwidth limited pump pulses and 24.5 pJ of coupled pulse energy is shown in Fig. 23(b) (left axis). The simulated spectrum corresponds closely with our experimental spectrum and displays a high degree of coherence over the entire spectral bandwidth, Fig. 23(b) (right axis). In order to experimentally characterize the coherence of the generated SC we perform a spectral interference measurement [105,106] in which the output from the waveguide is sent to a free-space asymmetric Michelson interferometer. One arm of the interferometer is chosen to provide a delay corresponding to the pulse period. This allows for interference between adjacent pulses, creating interference fringes on the optical spectrum analyzer when the SC generated by subsequent pulses are coherent. A single sweep of the OSA records the ensemble average of >109 interference events, from which the first-order mutual coherence $g_{12}^{(1)}(\lambda)$ may be calculated according to [105],

$$\left|g_{12}^{(1)}(\lambda)\right| = \frac{V(\lambda)[I_1(\lambda) + I_2(\lambda)]}{2[I_1(\lambda)I_2(\lambda)]^{1/2}} \quad (14)$$

where $I_1(\lambda)$ and $I_2(\lambda)$ are the measured spectral intensities from each arm of the interferometer, and $V(\lambda)$ denotes the fringe visibility, which is given by the maximum and minimum fringe intensity as $V(\lambda) = [I_{\max}(\lambda) - I_{\min}(\lambda)]/[I_{\max}(\lambda) + I_{\min}(\lambda)]$ [107].

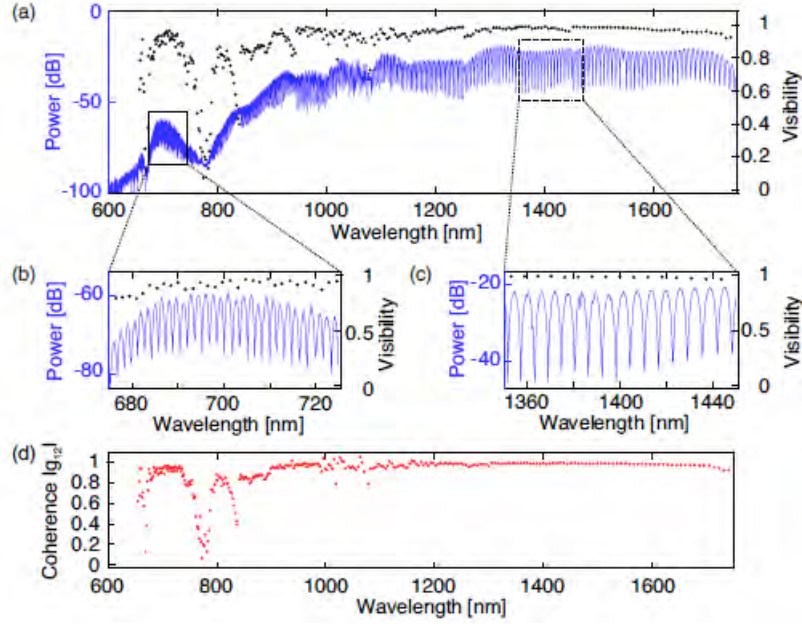


Figure 24. (a) Left axis: Experimental spectral interference measurement (blue) shows high extinction fringes over most of the SC bandwidth. Right axis: visibility (black) is close to unity over much of the wavelength range. (b) Magnified view of interference fringes and extracted visibility at 700 nm and (c) 1400 nm. (d) Extracted coherence (red) is close to unity over much of the wavelength range.

For the coherence measurement the temporal delay between interfering pulses is selected to give adequate resolution (fringe spacing) over the entire wavelength range. Light output from the interferometer is collimated into a fiber and sent to the OSA. We use a fiber that is single-mode at 1550 nm for measurement of wavelengths longer than 1250 nm and a fiber that is single-mode at 1060 nm for measurements performed below 1250 nm. This smaller core fiber ensures the spatial overlap between the interfering pulses at wavelengths longer than the cutoff wavelength. The spectral interference measurement is performed in 100-nm steps with optimization of the collimation and the alignment of the output for each wavelength region. The interference measurement is shown on the left axis of Fig. 24(a). As seen in Fig. 24(a) (left axis), interference fringes exist over the entire spectral range above the noise floor. The right axis of Fig. 24(a) gives the extracted visibility, which is near unity for the majority of the SC bandwidth. For measurements taken below the cutoff wavelength of the 1060 nm single-mode fiber (~ 890 nm), the multi-mode nature of the fiber leads to a sensitivity to the fiber collimator input coupling. This effect is seen in the reduction of the fringe extinction from 740 – 840 nm and in a decrease of the visibility, especially at the edges of the measurement range. Over the wavelength range from 840 – 1750 nm the average visibility is 0.94. This high average visibility results from the high degree of phase coherence that exists between interfering pulses. As seen in Eq. (14), the visibility is equal to the first-order mutual coherence with the inclusion of a normalization factor that takes into account any differences in the intensities of the individual interferometer arms. Importantly, we measure visibility near unity at spectral regions that are an octave apart, which enables f - $2f$ interferometry and detection of the f_{ceo} of the modelocked laser source. A magnified view of these spectral regions at 700 nm and 1400 nm is shown in the insets of Fig. 24(b) and

(c). We measure an average visibility of 0.9 over the wavelength range from 675 nm – 725 nm, and an average visibility of 0.99 over the wavelength range from 1350 – 1450 nm. For some wavelength regions we are limited by the signal-to-noise ratio of the measured SC spectrum and thus could not extract the visibility. Lastly, we calculate the first-order mutual coherence. The calculated coherence shown in Fig. 24(d) closely resembles the extracted visibility with slight differences due to the normalization factor. In the spectral region surrounding the pump wavelength we observe modulations in the measured intensity in the delay arm and reference arm of the interferometer, which distorts the coherence calculation.

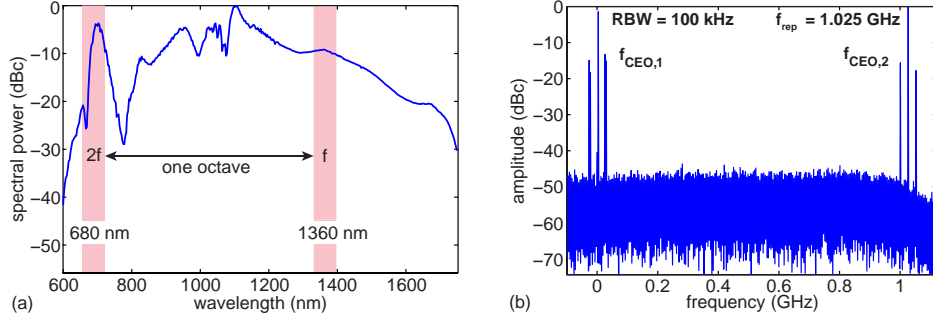


Figure 25. (a) Supercontinuum spectrum obtained with 37 mW of coupled average power at 1.025 GHz. (b) Microwave spectrum showing the pulse repetition rate f_{rep} and the CEO beat frequencies $f_{\text{CEO},1}$ and $f_{\text{CEO},2}$ at 0.024 GHz and 1.001 GHz, respectively.

Finally, we detect the frequency comb offset, given by the carrier envelope offset (CEO) frequency, of the SESAM-modelocked diode-pumped Yb:CALGO laser [108]. In order to detect the CEO frequency of our lasers, the waveguide output is collimated and sent into a quasi-common path f -to- $2f$ interferometer. The spectral portion around 1360 nm is frequency doubled in a periodically poled lithium niobate (PPLN) crystal and then collinearly recombined in space and time with the 680-nm components of the supercontinuum. After passing through a bandpass filter, the beat signals are detected using a gigahertz avalanche photodiode (APD) and displayed on a microwave spectrum analyzer (MSA). In Fig. 25, we show the detected f_{CEO} beat signals and the corresponding SC spectra that were used for f -to- $2f$ interferometry. The depicted data was obtained with 30 pJ (36 pJ) of coupled pulse energy, corresponding to 337 W (345 W) of peak power for the 100-MHz (1-GHz) laser. A signal-to-noise ratio (SNR) of > 30 dB with a FWHM of ≈ 2 MHz is obtained for the CEO beat of the 1-GHz laser. The SNR of the CEO beats is sufficient for additional microwave signal processing, i.e. it will allow us to perform further characterization of the CEO noise properties in the near future. Furthermore, the fact that the CEO beat center frequency can be shifted over a substantial range when adjusting the laser pump power is an essential requirement for ultimately stabilizing the CEO frequency to an external radio-frequency reference by providing feedback to the current of the pump diode.

11. References

- [1] S. T. Cundiff and J. Ye, “Colloquium: Femtosecond optical frequency combs,” *Rev. Mod. Phys.* **75**, S. T 325 (2003).
- [2] Th. Udem, R. Holzwarth, and T. W. Hänsch, “Optical frequency metrology,” *Nature* **416**, 233 (2002).
- [3] Z. Jiang, D. E. Leaird, and A. M. Weiner, “Line-by-line pulse shaping control for optical arbitrary waveform generation,” *Opt. Express* **13**, 10431 (2005).
- [4] T. Steinmetz, *et al.*, “Laser frequency combs for astronomical observations,” *Science* **321**, 1335 (2008).
- [5] S. T. Cundiff, J. Ye, and J. L. Hall, “Optical frequency synthesis based on mode-locked lasers,” *Rev. Sci. Instrum.* **72**, 3749 (2001).
- [6] P. Del Haye, *et al.*, “Optical frequency comb generation from a monolithic microresonator,” *Nature* **450**, 1214 (2007).
- [7] T. J. Kippenberg, R. Holzwarth, and S. A. Diddams, “Microresonator-based optical frequency combs,” *Science* **339**, 555 (2011).
- [8] J. S. Levy, *et al.*, A. L. Gaeta, and M. Lipson, “CMOS-compatible multiple-wavelength oscillator for on-chip optical interconnects,” *Nature Photonics* **4**, 37 (2010).
- [9] M. A. Foster, *et al.*, M. Lipson, and A. L. Gaeta, “Silicon-based monolithic optical frequency comb source,” *Opt. Express* **19**, 14233 (2011).
- [10] Y. Okawachi, *et al.*, M. Lipson, and A. L. Gaeta, “Octave-spanning frequency comb generation in a silicon nitride chip,” *Opt. Lett.* **36**, 3398 (2011).
- [11] K. Saha, *et al.*, M. Lipson, and A. L. Gaeta, “Modelocking and femtosecond pulse generation in chip-based frequency combs,” *Opt. Express* **21**, 1335 (2013).
- [12] A. B. Matsko, *et al.*, “Mode-locked Kerr frequency combs,” *Opt. Lett.* **36**, 2845 (2011).
- [13] M. Haelterman, S. Trillo, and S. Wabnitz, “Dissipative Modulation Instability in a Nonlinear Dispersive Ring Cavity,” *Opt. Commun.* **91**, 401 (1992).
- [14] S. Coen, H. G. Randle, T. Sylvestre, and M. Erkintalo, “Modeling of octave-spanning Kerr frequency combs using a generalized mean-field Lugiato-Lefever model,” *Opt. Lett.* **38**, 37 (2013).
- [15] L. A. Lugiato and R. Lefever, “Spatial Dissipative Structures in Passive Optical-Systems,” *Phys. Rev. Lett.* **58**, 2209 (1987).
- [16] M. R. E. Lamont, Y. Okawachi, and A. L. Gaeta, “Route to stabilized ultrabroadband microresonator-based frequency combs,” *Opt. Lett.* **38**, 3478 (2013).
- [17] J. M. Dudley, G. Genty, and S. Coen, “Supercontinuum generation in photonic crystal fiber,” *Rev. Mod. Phys.* **78**, 1135 (2006).
- [18] T. Herr, *et al.*, “Universal formation dynamics and noise of Kerr-frequency combs in microresonators,” *Nature Photon.* **6**, 480 (2012).
- [19] A. B. Matsko, W. Liang, A. A. Savchenkov, and L. Maleki, “Chaotic dynamics of frequency combs generated with continuously pumped nonlinear microresonators,” *Opt. Lett.* **38**, 525 (2013).

- [20] Y. Okawachi, *et al.*, M. Lipson, and A. L. Gaeta, “Bandwidth shaping of microresonator-based frequency combs via dispersion engineering,” *Opt. Lett.* **39**, 3535 (2014).
- [21] V. Torres-Company, D. Castelló-Lurbe, and E. Silvestre, “Comparative analysis of spectral coherence in microresonator frequency combs,” *Opt. Express* **22**, 4678 (2014).
- [22] M. Haelterman, S. Trillo, and S. Wabnitz, “Additive-modulation-instability ring laser in the normal dispersion regime of a fiber,” *Opt. Lett.* **17**, 745 (1992).
- [23] T. Hansson, D. Modotto, and S. Wabnitz, “Dynamics of the modulational instability in microresonator frequency combs,” *Phys. Rev. A* **88**, 023819 (2013).
- [24] K. Luke, A. Dutt, C. B. Poitras, and M. Lipson, “Overcoming Si_3N_4 film stress limitations for high quality factor ring resonators,” *Opt. Express* **21**, 22829 (2013).
- [25] S. Coen and M. Erkintalo, “Universal scaling laws of Kerr frequency combs,” *Opt. Lett.* **38**, 1790 (2013).
- [26] T. Kerr, *et al.*, “Temporal solitons in optical microresonators,” *Nature Photon.* **8**, 145 (2013).
- [27] S. Wang, H. Guo, X. Bai, and X. Zeng, “Broadband Kerr frequency combs and intracavity soliton dynamics influenced by high-order cavity dispersion,” *Opt. Lett.* **39**, 2880 (2014).
- [28] M. A. Foster, A. C. Turner, M. Lipson, and A. L. Gaeta, “Nonlinear optics in photonic nanowires,” *Opt. Express* **16**, 1300 (2008).
- [29] Y. Kuramoto, *Chemical Oscillations, Waves and Turbulence* (Springer-Verlag, 1984).
- [30] S. H. Strogatz, “From Kuramoto to Crawford: exploring the onset of synchronization in populations of coupled oscillators,” *Physica D* **143**, 1 (2000).
- [31] A. E. Motter, S. A. Myers, M. Anghel, T. Nishikawa, “Spontaneous synchrony in power-grid networks,” *Nature Phys.* **9**, 191 (2013).
- [32] T. Womelsdorf, *et al.*, “Modulation of neuronal interactions through neuronal synchronization,” *Science* **316**, 1609 (2007).
- [33] I. Z. Kiss, Y. Zhai, J. L. Hudson, “Emerging coherence in a population of chemical oscillators,” *Science* **296**, 1676 (2002).
- [34] K. Wiesenfeld, P. Colet, and S. H. Strogatz, “Synchronization transitions in a disordered Josephson series array,” *Phys. Rev. Lett.* **76**, 404 (1996).
- [35] G. Kozyreff, A. G. Vladimirov, and P. Mandel, “Global coupling with time delay in an array of semiconductor lasers,” *Phys. Rev. Lett.* **85**, 3809 (2000).
- [36] F. Leo, *et al.*, “Temporal cavity solitons in one-dimensional Kerr media as bits in an all-optical buffer,” *Nature Photon.* **4**, 471 (2010).
- [37] W. J. Firth and C. O. Weiss, “Cavity and feedback solitons,” *Opt. Photon. News* **13**, 54 (2002).
- [38] Y. H. Wen, *et al.*, and A. L. Gaeta, “Self-organization in soliton modelocked parametric frequency combs,” arXiv: 1412.0119 (2014).
- [39] T. J. Kippenberg, S. M. Spillane, and K. J. Vahala, “Modal coupling in traveling-wave resonators,” *Opt. Lett.* **27**, 1669 (2002).

- [40] T. Carmon, *et al.*, “Static envelope patterns in composite resonances generated by level crossing in optical toroidal microcavities,” *Phys. Rev. Lett.* **100**, 103905 (2008).
- [41] A. A. Savchenkov, *et al.*, “Kerr frequency comb generation in overmoded resonators,” *Opt. Express* **20**, 27290 (2012).
- [42] T. Herr, *et al.*, “Mode spectrum and temporal soliton formation in optical microresonators,” *Phys. Rev. Lett.* **113**, 123901 (2014).
- [43] Y. Liu, *et al.*, “Investigation of mode interaction in optical microresonators for Kerr frequency comb generation,” *arXiv:1402.5686* (2014).
- [44] I. S. Grudinin, L. Baumgartel, and N. Yu, “Impact of cavity spectrum on span in microresonator frequency combs,” *Opt. Express* **21**, 26929 (2013).
- [45] F. Sedlmeir, *et al.*, “Experimental characterization of an uniaxial angle cut whispering gallery mode resonator,” *Opt. Express* **21**, 23942 (2013).
- [46] I. S. Grudinin, L. Baumgartel, and N. Yu, “Frequency comb from a microresonator with engineered spectrum,” *Opt. Express* **20**, 6604 (2012).
- [47] X. Xue, *et al.*, “Mode interaction aided soft excitation of dark solitons in normal dispersion microresonators and offset-frequency tunable Kerr combs,” *arXiv:1404.2865* (2014).
- [48] S.-W. Huang, *et al.*, “Direct generation of 74-fs mode-locking from on-chip normal dispersion frequency combs,” *arXiv:1404.3256* (2014).
- [49] W. W. Lui, T. Hirono, K. Yokoyama, and W. Huang, “Polarization Rotation in Semiconductor Bending Waveguides: A Coupled-Mode Theory Formulation,” *J. Lightwave Technol.* **16**, 929 (1998).
- [50] N. Somasiri, and B. M. A. Rahman, “Polarization Crosstalk in High Index Contrast Planar Silica Waveguides With Slanted Sidewalls,” *J. Lightwave Technol.* **21**, 54 (2003).
- [51] F. Morichetti, A. Melloni, M. Martinelli, “Modelling of Polarization Rotation in Bent Waveguides,” 2006 International Conference on Transparent Optical Networks **4**, 261 (2006).
- [52] S. Ramelow, *et al.*, M. Lipson, and A. L. Gaeta, “Strong polarization mode coupling in microresonators,” *Opt. Lett.* **39**, 5134 (2014).
- [53] P. Del’Haye, *et al.*, “Octave spanning tunable frequency comb from a microresonator,” *Phys. Rev. Lett.* **107**, 063901 (2011).
- [54] H. Jung, *et al.*, “Optical frequency comb generation from aluminum nitride microring resonator,” *Opt. Lett.* **38**, 2810 (2013).
- [55] C. Bao, *et al.*, “Nonlinear conversion efficiency in Kerr frequency comb generation,” *Opt. Lett.* **39**, 6126 (2014).
- [56] L. Zhou and A. W. Poon, “Electrically reconfigurable silicon microring resonator-based filter with waveguide-coupled feedback,” *Opt. Express* **15**, 9194 (2007).
- [57] M. A. Popović, *et al.*, “Transparent wavelength switching of resonant filters,” in “Conference on Lasers and Electro-Optics/Quantum Electronics and Laser Science Conference and Photonic Applications Systems Technologies,” (Optical Society of America, 2007), OSA Technical Digest Series (CD), p. CPDA2.

- [58] L. Chen, N. Sherwood-Droz, and M. Lipson, "Compact bandwidth-tunable microring resonators," *Opt. Lett.* **32**, 3361 (2007).
- [59] S. A. Miller, *et al.*, and M. Lipson, "Tunable frequency combs based on dual microring resonators," *Opt. Express* **23**, 21527 (2015).
- [60] A. C. Turner, C. Manolatou, B. S. Schmidt, M. Lipson, M. A. Foster, J. E. Sharping, and A. L. Gaeta, "Tailored anomalous group-velocity dispersion in silicon channel waveguides," *Opt. Express* **14**, 4357 (2006).
- [61] T. Carmon, L. Yang, and K. J. Vahala, "Dynamical thermal behavior and thermal self-stability of microcavities," *Opt. Express* **12**, 4742-4750 (2004).
- [62] M. Peccianti, *et al.*, "Demonstration of a stable ultrafast laser based on a nonlinear microcavity," *Nature Comm.* **3**, 765 (2012).
- [63] A. Pasquazi, *et al.*, "Self-locked optical parametric oscillation in a CMOS compatible microring resonator: a route to robust optical frequency comb generation on a chip," *Opt. Express* **21**, 13333 (2013).
- [64] N. A. Cholan, *et al.*, "Multi-wavelength generation by self-seeded four-wave mixing", *Opt. Express* **21**, 6131 (2013).
- [65] T. Bajraszewski, *et al.*, "Improved spectral optical coherence tomography using optical frequency comb," *Opt. Express* **16**, 4163 (2008).
- [66] K. Saha, *et al.*, M. Lipson, and A. L. Gaeta, "Broadband parametric frequency comb generation with a 1- μ m pump source," *Opt. Express* **20**, 26935 (2012).
- [67] K. Luke, *et al.*, A. L. Gaeta, and M. Lipson, "Broadband microresonator-based parametric frequency comb near visible wavelengths," in *CLEO: 2014*, OSA Technical Digest (online) (Optical Society of America, 2014), paper FW1D.3.
- [68] J. S. Levy, M. A. Foster, A. L. Gaeta, and M. Lipson, "Harmonic generation in silicon nitride ring resonators," *Opt. Express* **19**, 11415 (2011).
- [69] T. Ning, *et al.*, "Strong second-harmonic generation in silicon nitride films," *Appl. Phys. Lett.* **100**, 161902 (2012).
- [70] D. F. Logan, *et al.*, "Harnessing second-order optical nonlinearities at interfaces in multilayer silicon-oxy-nitride waveguides," *Appl. Phys. Lett.* **102**, 061106 (2013).
- [71] E. F. Pecora, A. Capretti, G. Miano, and L. D. Negro, "Generation of second harmonic radiation from sub-stoichiometric silicon nitride thin films," *Appl. Phys. Lett.* **102**, 141114 (2013).
- [72] A. Kitao, K. Imakita, I. Kawamura, and M. Fujii, "An investigation into second harmonic generation by Si-rich SiNx thin films deposited by RF sputtering over a wide range of Si concentrations," *J. Phys. Appl. Phys.* **47**, 215101 (2014).
- [73] M. Cazzanelli, *et al.*, "Second-harmonic generation in silicon waveguides strained by silicon nitride," *Nat Mater* **11**, 148 (2012).
- [74] D. J. Moss, R. Morandotti, A. L. Gaeta, and M. Lipson, "New CMOS-compatible platforms based on silicon nitride and Hydex for nonlinear optics," *Nat. Photonics* **7**, 597 (2013).

- [75] S. B. Papp and S. A. Diddams, "Spectral and temporal characterization of a fused-quartz-microresonator optical frequency comb," *Phys. Rev. A* **84**, 053833 (2011).
- [76] M. M. Milošević, *et al.*, "Rib waveguides for mid-infrared silicon photonics," *J. Opt. Soc. Am. B* **26**, 1760 (2009).
- [77] F. Gholami, *et al.*, "Third-order nonlinearity in silicon beyond 2350 nm," *Appl. Phys. Lett.* **99**, 081102 (2011).
- [78] S. Pearl, N. Rotenberg, and H. M. van Driel, "Three photon absorption in silicon for 2300–3300 nm," *Appl. Phys. Lett.* **93**, 131102 (2008).
- [79] B. Desiatov, I. Goykhman, and U. Levy, "Demonstration of submicron square-like silicon waveguide using optimized LOCOS process," *Opt. Express* **18**, 18592 (2010).
- [80] A. Griffith, J. Cardenas, C. B. Poitras, and M. Lipson, "High quality factor and high confinement silicon resonators using etchless process," *Opt. Express* **20**, 21341 (2012).
- [81] H. Rong, *et al.*, "An all-silicon Raman laser," *Nature* **433**, 292 (2005).
- [82] A. C. Turner-Foster, *et al.*, A. L. Gatea, and M. Lipson, "Ultrashort free-carrier lifetime in low-loss silicon nanowaveguides," *Opt. Express* **18**, 3582 (2010).
- [83] R. A. Soref and B. R. Bennett, "Electrooptical effects in silicon," *IEEE J. Quantum Electron.* **23**, 123 (1987).
- [84] R. Claps, V. Raghunathan, D. Dimitropoulos, and B. Jalali, "Influence of nonlinear absorption on Raman amplification in silicon waveguides," *Opt. Express* **12**, 2774 (2004).
- [85] L. F. Mollenauer, R. H. Stolen, J. P. Gordon, and W. J. Tomlinson, "Extreme picosecond pulse narrowing by means of soliton effect in single-mode optical fibers," *Opt. Lett.* **8**, 289 (1983).
- [86] H. R. Telle, *et al.*, "Carrier-envelope offset phase control: A novel concept for absolute optical frequency measurement and ultrashort pulse generation," *Appl. Phys. B* **69**, 327 (1999).
- [87] R. Holzwarth, *et al.*, "Optical Frequency Synthesizer for Precision Spectroscopy," *Phys. Rev. Lett.* **85**, 2264 (2000).
- [88] I. Zeylikovich, V. Kartazayev, and R. R. Alfano, "Spectral, temporal, and coherence properties of supercontinuum generation in microstructure fiber," *J. Opt. Soc. Am. B.* **22**, 1453 (2005).
- [89] S. Schiller, "Spectrometry with frequency combs," *Opt. Lett.* **27**, 766 (2002).
- [90] I. Coddington, W. C. Swann, and N. R. Newbury, "Coherent Multiheterodyne Spectroscopy Using Stabilized Optical Frequency Combs," *Phys. Rev. Lett.* **100**, 013902 (2008).
- [91] F. Leo, *et al.*, "Dispersive wave emission and supercontinuum generation in a silicon wire waveguide pumped around the 1550 nm telecommunication wavelength," *Opt. Lett.* **39**, 3623 (2014).
- [92] B. Kuyken, *et al.*, "An octave-spanning mid-infrared frequency comb generated in a silicon nanophotonic wire waveguide," *Nat. Comm.* **6**, 6310 (2015).
- [93] R. K. W. Lau, *et al.*, M. Lipson, and A. L. Gaeta, "Octave-spanning mid-infrared supercontinuum generation in silicon nanowaveguides," *Opt. Lett.* **39**, 4518 (2014).

- [94] F. Leo, *et al.*, “Generation of coherent supercontinuum in a-Si:H waveguides: experiment and modeling based on measured dispersion profile,” *Opt. Express* **22**, 28997 (2014).
- [95] D. Y. Oh, *et al.*, “Supercontinuum generation in an on-chip silica waveguide,” *Opt. Lett.* **39**, 1046 (2014).
- [96] D. Duchesne, *et al.*, “Supercontinuum generation in a high index doped silica glass spiral waveguide,” *Opt. Express* **18**, 923 (2010).
- [97] R. Halir, *et al.*, M. Lipson, and A. L. Gaeta, “Ultrabroadband supercontinuum generation in a CMOS-compatible platform,” *Opt. Lett.* **37**, 1685 (2012).
- [98] J. M. Chavez Boggio, *et al.*, “Dispersion engineered silicon nitride waveguides by geometrical and refractive-index optimization,” *J. Opt. Soc. Am. B.* **31**, 2846 (2014).
- [99] H. Zhao, *et al.*, “Visible-to-near-infrared octave spanning supercontinuum generation in a silicon nitride waveguide,” *Opt. Lett.* **40**, 2177 (2015).
- [100] J. P. Epping, *et al.*, “On-chip visible-to-infrared supercontinuum generation with more than 495 THz spectral bandwidth,” *Opt. Express* **23**, 19596 (2015).
- [101] R. Salem, *et al.*, M. Lipson, A. L. Gaeta, “Octave-spanning supercontinuum generation in a silicon nitride waveguide pumped by a femtosecond fiber laser at 1.9 μm ,” in *CLEO: 2014, OSA Technical Digest (online)* (Optical Society of America, 2015), paper STu1I.7.
- [102] A. R. Johnson, *et al.*, F. W. Wise, M. Lipson, U. Keller, and A. L. Gaeta, “Octave-spanning coherent supercontinuum generation in a silicon nitride waveguide,” (*submitted* 2015).
- [103] A. Klenner, S. Schilt, T. Südmeyer, and U. Keller, “Gigahertz frequency comb from a diode-pumped solid-state laser,” *Opt. Express* **22**, 31008 (2014).
- [104] A. Ruehl, *et al.*, “Ultrabroadband coherent supercontinuum frequency comb,” *Phys. Rev.* **84**, 011806 (2011).
- [105] X. Gu, *et al.*, “Experimental studies of the coherence of microstructure-fiber supercontinuum,” *Opt. Express* **11**, 2697 (2011).
- [106] F. Lu and W. H. Knox, “Generation of a broadband continuum with high spectral coherence in tapered single-mode optical fibers,” *Opt. Express* **12**, 347 (2004).
- [107] J. W. Nicholson and M. F. Yan, “Cross-coherence measurements of supercontinua generated in highly-nonlinear, dispersion shifted fiber at 1550 nm,” *Opt. Express* **12**, 679 (2004).
- [108] A. S. Mayer, *et al.*, M. Lipson, A. L. Gaeta, and U. Keller, “Frequency comb offset detection using supercontinuum generation in silicon nitride waveguides,” *Opt. Express* **23**, 15440 (2015).

1.

1. Report Type

Final Report

Primary Contact E-mail

Contact email if there is a problem with the report.

a.gaeta@cornell.edu

Primary Contact Phone Number

Contact phone number if there is a problem with the report

607-592-8863

Organization / Institution name

Cornell University

Grant/Contract Title

The full title of the funded effort.

SILICON-CHIP-BASED OPTICAL FREQUENCY COMBS

Grant/Contract Number

AFOSR assigned control number. It must begin with "FA9550" or "F49620" or "FA2386".

FA9550-12-1-0377

Principal Investigator Name

The full name of the principal investigator on the grant or contract.

Alexander Gaeta

Program Manager

The AFOSR Program Manager currently assigned to the award

Enrique Parra

Reporting Period Start Date

07/15/2012

Reporting Period End Date

07/14/2015

Abstract

We have theoretically and experimentally investigated the dynamics of frequency comb generation in silicon-based microresonators. In this system, the parametric gain associated with the nonlinear process of four-wave mixing leads to parametric oscillation and generation of signal/idler sidemodes.

This report describes our results that further develop the parametric comb technology. We theoretically investigate comb generation and modelocking dynamics, and the connection to concepts of synchronization and self-organization. We also investigated mode-crossings in microresonators and tunable coupling, and their impact on comb formation. We studied comb generation without an external pump laser. In addition, we explored comb generation at other pump wavelengths using dispersion engineering. Finally, we investigated comb generation via coherent supercontinuum generation in silicon nitride waveguides.

Our research effort illustrates that the silicon-based platform offers a high potential as a platform for robust, integrated, chip-scale comb source. Since the dispersion of the system can be readily tailored through waveguide cross-section engineering, the platform offers flexibility in operating wavelength and bandwidth. The developments made here are a significant step towards the development of chip-based frequency combs that can operate in real-world sensing and spectroscopy, for optical clocks, and for frequency

metrology applications.

Distribution Statement

This is block 12 on the SF298 form.

Distribution A - Approved for Public Release

Explanation for Distribution Statement

If this is not approved for public release, please provide a short explanation. E.g., contains proprietary information.

SF298 Form

Please attach your [SF298](#) form. A blank SF298 can be found [here](#). Please do not password protect or secure the PDF. The maximum file size for an SF298 is 50MB.

[SF298_form_Cornell.pdf](#)

Upload the Report Document. File must be a PDF. Please do not password protect or secure the PDF. The maximum file size for the Report Document is 50MB.

[Comb_Final_Report_AFOSR.pdf](#)

Upload a Report Document, if any. The maximum file size for the Report Document is 50MB.

Archival Publications (published) during reporting period:

K. Saha, et al., M. Lipson, and A. L. Gaeta, "Broadband parametric frequency comb generation with a 1- μ m pump source," Opt. Express 20, 26935 (2012).

K. Saha, et al., M. Lipson, and A. L. Gaeta, "Modelocking and femtosecond pulse generation in chip-based frequency combs," Opt. Express 21, 1335 (2013).

K. Luke, A. Dutt, C. B. Poitras, and M. Lipson, "Overcoming Si₃N₄ film stress limitations for high quality factor ring resonators," Opt. Express 21, 22829 (2013).

Y. Okawachi, et al., M. Lipson, and A. L. Gaeta, "Bandwidth shaping of microresonator-based frequency combs via dispersion engineering," Opt. Lett. 39, 3535 (2014).

S. Ramelow, et al., M. Lipson, and A. L. Gaeta, "Strong polarization mode coupling in microresonators," Opt. Lett. 39, 5134 (2014).

R. K. W. Lau, et al., M. Lipson, and A. L. Gaeta, "Octave-spanning mid-infrared supercontinuum generation in silicon nanowaveguides," Opt. Lett. 39, 4518 (2014).

Y. H. Wen, et al., and A. L. Gaeta, "Self-organization in soliton modelocked parametric frequency combs," arXiv: 1412.0119 (2014).

S. A. Miller, et al., and M. Lipson, "Tunable frequency combs based on dual microring resonators," Opt. Express 23, 21527 (2015).

A. S. Mayer, et al., M. Lipson, A. L. Gaeta, and U. Keller, "Frequency comb offset detection using supercontinuum generation in silicon nitride waveguides," Opt. Express 23, 15440 (2015).

Changes in research objectives (if any):

None

Change in AFOSR Program Manager, if any:

Extensions granted or milestones slipped, if any:

AFOSR LRIR Number

LRIR Title

Reporting Period

Laboratory Task Manager

Program Officer

Research Objectives

Technical Summary

Funding Summary by Cost Category (by FY, \$K)

	Starting FY	FY+1	FY+2
Salary			
Equipment/Facilities			
Supplies			
Total			

Report Document

Report Document - Text Analysis

Report Document - Text Analysis

Appendix Documents

2. Thank You

E-mail user

Oct 14, 2015 11:41:43 Success: Email Sent to: a.gaeta@cornell.edu